Applied Thermal Engineering 246 (2024) 122934

Contents lists available at ScienceDirect

Applied Thermal Engineering

journal homepage: www.elsevier.com/locate/apthermeng

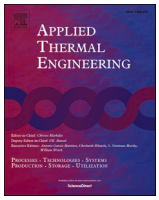

Research Paper

Experimental heat transfer results and flow visualization of horizontal Near-Saturated liquid nitrogen flow boiling in uniformly heated circular tube under Earth gravity

Sunjae Kim [a], Nishad Damle [a], Issam Mudawar [a,*], Jason Hartwig [b]

[a] Purdue University Boiling and Two-Phase Flow Laboratory (PU-BTPFL), School of Mechanical Engineering, Purdue University, 585 Purdue Mall, West Lafayette, IN, 47907, U.S.A

[b] Fluids and Cryogenics Branch, NASA Glenn Research Center, 21000 Brookpark Rd, Cleveland, OH, 44135, U.S.A

ARTICLE INFO

Keywords:
Cryogens
Near Saturated Flow Boiling
Horizontal Flow
Terrestrial gravity

ABSTRACT

This study investigates 1-g_e horizontal flow boiling of liquid nitrogen with a near-saturated inlet along a circular tube of dimensions 8.5-mm inner diameter and 680-mm heated length. Experiments are conducted using a payload developed for eventual parabolic flight experiments. The operating parameters varied are mass velocity of 406.76–1572.77 kg/m^{2}s, inlet quality of −0.05 to −0.01, and inlet pressure of 336.29–493.07 kPa. High speed video recordings are presented to explain two-phase flow structure and regime transitions which are visualized through a transparent tube in a visualization section situated downstream of the heated tube. Recognized flow patterns are bubbly, plug, slug, stratified annular, and annular. Heat transfer results are presented and discussed in terms of flow boiling curve trends, streamwise wall temperature profiles, streamwise heat transfer coefficient (HTC) profiles, and average HTCs. Previous HTC correlations are evaluated against the measured HTC data, of which two are identified for superior accuracy in predicting cryogen data. Finally, this study confirms the reliability and readiness of the payload for subsequent parabolic flight experiments intended for acquisition of microgravity data.

1. INTRODUCTION

1.1. Importance of cryogenic flow boiling physics in space applications

Historically, cryogenic fluids, which are substances that exist as liquids at extremely low temperatures, have been employed in a broad variety of applications throughout industry. As a few examples: liquid nitrogen (LN_2) is used to fast freeze food, preserve tissues and blood, and eliminate targeted tissues in cryosurgery, liquid oxygen (LOX) is used in life support systems and fuel cells, and liquid hydrogen (LH_2) as coolant for superconducting magnets.

Cryogenic propellants, renowned for their exceptional performance in specific impulse and energy density compared to conventional propellants, have attracted considerable attention in various applications, notably in space exploration. Furthermore, a NASA roadmap recently highlighted cryogenic fluid management (CFM) technologies as crucial for maximizing the efficient utilization of cryogenic propellants in future long-duration missions [1].

For missions venturing beyond low Earth orbit (LEO), the establishment of cryogenic fuel depot systems will be essential to provide the neccessary propellant for maneuvering and other in-space activities. These systems typically involve the transfer of cryogenic liquids from large-volume storage tanks to smaller tanks or spacecrafts [2]. During the fuel transfer, it is crucial to ensure that the system hardware, including the feed line, flow components, and various storage tanks, be cooled down to cryogenic temperatures before providing vapor-free liquid. This cooling process is commonly accomplished through flow boiling heat transfer, whereby a portion of the propellant is allowed to boil, thus extracting thermal energy from the system walls [3]. This underscores the importance of comprehending the fluid physics of cryogenic flow boiling. The significance of CFM technology extends beyond propellant transfer or storage for fuel depots, particularly in the context of developing Nuclear Thermal Propulsion (NTP) powered vehicles. NTP, whether intended to provide thrust for spacecraft maneuvering between orbits or operating as a dual-mode system offering both power and propulsion capabilities, offers substantial architectural advantages for exploration missions and reusable in-space transportation

* Corresponding author.
E-mail address: mudawar@ecn.purdue.edu (I. Mudawar).

https://doi.org/10.1016/j.applthermaleng.2024.122934
Received 29 October 2023; Received in revised form 14 February 2024; Accepted 11 March 2024
Available online 13 March 2024

Nomenclature

D	diameter (mm)
f	friction factor
F	enhancement factor
G	mass velocity (kg/m^2.s)
g_e	Earth gravity (m/s^2)
h	enthalpy (J/kg); heat transfer coefficient (kW/m^{2}K)
h_{fg}	latent heat of vaporization (J/kg)
k	thermal conductivity (W/m•K)
L_e	entrance length (mm)
L_H	heated length (mm)
L_{sp}	single-phase liquid length
N	number of data points
P	pressure (Pa)
Pr	Prandtl number
q''	heat flux (W/m^2)
S	suppression factor
T	temperature (°C, K)
t	time (s)
Th	wall thickness (mm)
x_e	thermodynamic equilibrium quality
X_{tt}	Lockhart-Martinelli parameter
z	axial coordinate (m)

Greek symbols

α	volume of fraction; void fraction
μ	dynamic viscosity (kg/m•s)
ρ	density (kg/m^3)
σ	surface tension (N/m)

Subscripts

avg	average
cb	convective boiling
f	liquid
fo	liquid only
g	vapor
i	inner; thermocouple indicator
in	inlet
meas	measured
nb	nucleate boiling
o	outer
out	outlet
pb	pool boiling
pred	predicted
s	solid wall
sat	saturation
sc	subcooling
sp	single phase liquid
tp	two-phase
w	inner wall
z	local

Acronyms

CHF	critical heat flux
HTC	heat transfer coefficient
HV	hand (ball) valve
ISS	International Space Station
LCH_4	liquid methane
LFP	Leidenfrost point
LH_2	liquid hydrogen
LHe	liquid helium
LN_2	liquid nitrogen
LOX	liquid oxygen
MAE	mean absolute error
NB	nucleate boiling
ONB	onset of nucleate boiling
ONBD	onset of departure from nucleate boiling
SV	solenoid valve

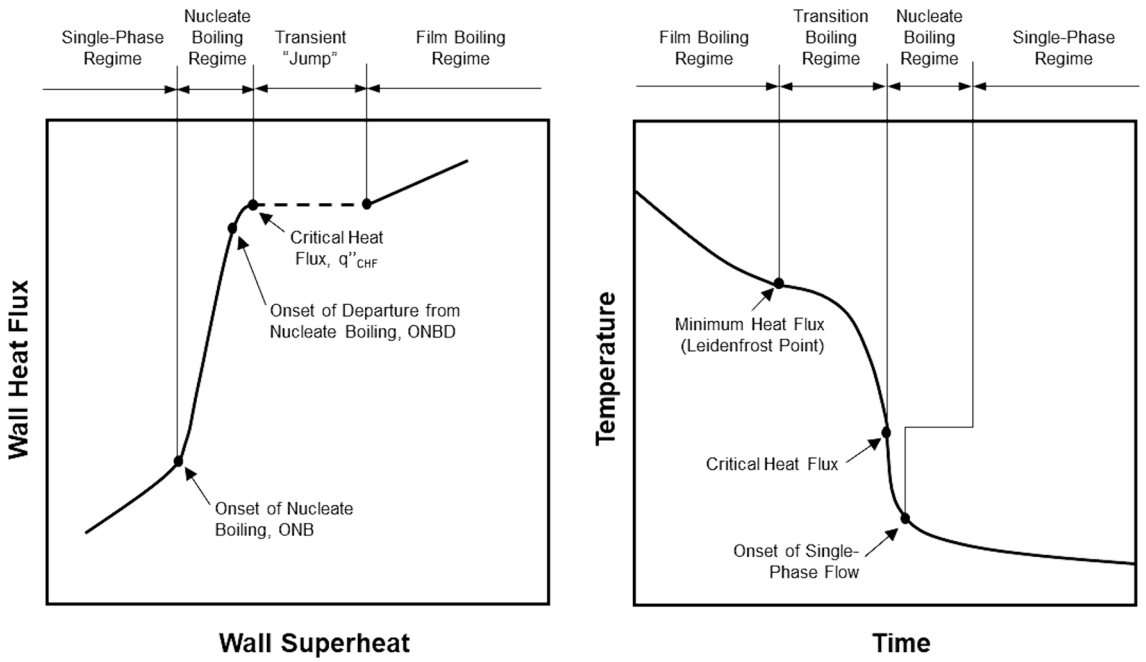

Fig. 1. Schematics of flow boiling curves for (a) heating and (b) quenching experiments.

Table 1
Summary of previous cryogenic flow boiling experiments.

Authors	Year	Fluid	D_i [mm]	L_h [m]	Flow Orientation	Exp. Method	Gravity condition	Flow Visualization	Remarks
Burke et al. [5]	1960	LN_2	47.5	18.3 30.5 53.3	Horizontal	Quenching	Earth gravity	None	• Sight glass installed but no flow images are reported
Bronson et al. [6]	1962	LH_2	34.9	15.2	Horizontal	Quenching	Earth gravity	None	• Identical glass mock-up utilized to visualize the flow pattern but no flow images are reported • Prevalent stratified flow regimes observed during chilldown
Brennan et al. [7]	1966	LN_2 LH_2	15.9	61.0	Horizontal	Quenching	Earth gravity	None	• Very long chilldown length
Velat [8]	2004	LN_2	12.7	N/A	Horizontal	Quenching	Earth gravity	Reported	• Pyrex glass adopted to visualize chilldown flow patterns • Quenching front demarcates transition from FB to NB • Confirmed the prevalence of stratified/wavy flow structures
Kawanami et al. [9]	2007	LN_2	7 10 13.6	0.15	Vertical Up Vertical Down	Quenching	Earth gravity	Reported	• Critical heat flux (CHF) reported for vertical upflow and downflow • Minimum heat flux (MHF) reported for vertical upflow and downflow • Filamentary flow image reported for vertical downflow chilldown
Kawanami et al. [10]	2007	LN_2	7	0.05	–	Quenching	Microgravity (drop tower)	Reported	• Enhanced heat transfer efficiency under μg • Increased quench from velocity • Less effect of gravity on HTC under high mass velocity
Yuan et al. [11]	2008	LN_2	11.1	0.254	–	Quenching	Microgravity (drop tower)	Reported	• Max. 20 % degradation of heat transfer efficiency under μg • Axisymmetric inverted annular flow (liquid at the core) • Longer chilldown time in μg
Hu et al. [12]	2012	LN_2	8.0	0.254	Vertical Up Vertical Down	Quenching	Earth gravity	Reported	• Faster chilldown time with vertical upflow than vertical downflow • Detailed flow regime observation • Faster quench front velocity with higher mass flow rate
Darr et al. [13,14]	2016	LN_2	11.68	0.572	Horizontal Vertical Up Vertical Down Inclined Up Inclined Down	Quenching	Earth gravity	None	• No flow visualization • Comprehensive parametric HTC trends reported for G, P_{in}, T_{sc}, and x_e • HTC hierarchy: Vertical Up > Horizontal > Vertical Down • Less effect of flow orientation on HTC under high mass velocity
Darr et al. [15]	2016	LN_2	11.68	0.572	–	Quenching	Microgravity (Parabolic flight)	None	• No flow visualization • Average 25 % degradation of heat transfer efficiency under μg • Less effect of gravity on HTC under high mass velocity • Faster chilldown time with higher mass flow rate
Lewis et al. [16]	1962	LN_2 LH_2	14.01	0.41	Vertical Up	Steady state heated tube	Earth gravity	None	• No flow visualization • Comprehensive tabulated data reported • Covered both pre-CHF and post-CHF
Papell et al. [17]	1966	LN_2	12.8	0.3	Vertical Up Vertical Down	Steady state heated tube	Earth gravity	None	• Significantly lower CHF for vertical downflow than vertical upflow • Less effect of flow orientation on CHF under high mass velocity • CHF instigated by local vapor accumulation
Simoneau and Simon [18]	1966	LN_2	25.4 x 25.4 (LxW)	0.12	Vertical Up Vertical Down	Steady state heated tube	Earth gravity	Reported	• Visually observed a significantly greater vapor accumulation in vertical downflow than in vertical upflow • No systematical acquisition of flow visualization results • Lower CHF for vertical downflow than vertical upflow
Steiner and Schlünder [19]	1976	LN_2	14	0.525	Horizontal	Steady state heated tube	Earth gravity	None	• Sight glass installed but no flow images are reported • Nucleate boiling dominant boiling regime confirmed (heat flux dependent) • Convective boiling regime not observed • Lower CHF than pool boiling CHF due to stratified flow patterns at CHF

(*continued on next page*)

Table 1 (*continued*)

Authors	Year	Fluid	D_i [mm]	L_h [m]	Flow Orientation	Exp. Method	Gravity condition	Flow Visualization	Remarks
Műller et al. [20]	1981	LN_2 LAr	14	0.525	Horizontal	Steady state heated tube	Earth gravity	None	• Sight glass installed but no flow images are reported • Nucleate boiling dominant boiling regime confirmed (heat flux dependent) • Increasing HTC with increasing mass velocity • Increasing HTC with increasing pressure
Klimenko and Sudarchikov [21]	1983	LN_2	10	1.85	Vertical Up	Steady state heated tube	Earth gravity	None	• Nucleate boiling dominant boiling regime confirmed (heat flux dependent) • Transition from NB to CB detected • No effect of mass velocity on HTC in vertical upflow • Increasing HTC with increasing pressure
Klimenko et al. [22]	1989	LN_2	4 9 14.1 15.8 18.9	0.45	Horizontal	Steady state heated tube	Earth gravity	None	• Tested multiple tube diameter, and revealed no influence of diameter on HTC • Effect of mass velocity more pronounced in horizontal flow • Detected stratified flow via circumferential temperature gradient
Qi et al. [23,24]	2007	LN_2	0.531 0.834 1.042 1.931	0.25	Vertical Up	Steady state heated tube	Earth gravity	None	• Microchannel two-phase flow • ONB correlation for LN_2 flow boiling proposed • Higher CHF compared to macro-channel CHF
Fu et al. [25]	2008	LN_2	1.93	0.1	Vertical Up	Steady state heated tube	Earth gravity	Reported	• Microchannel two-phase flow • Flow patters for LN2 flow boiling reported • Bubbly flow, slug flow, churn flow, and annular flow • Prevalence of annular flow covering the entire range of $x_e > 0.15$
Fang et al. [26]	2016	LN_2	11.9	1.45	Vertical Up	Steady state heated tube	Earth gravity	None	• Assumed existence of inverted annular flow which is not commonly reported from other LN_2 flow boiling experiments • Reported good prediction accuracy of the correlation developed by Liu and Winterton [48]

systems [4]. Such NTP systems use a nuclear reactor to heat a propellant, such as LH_2, which is then expelled out of a nozzle to produce thrust and also used as coolant for maintaining acceptable temperature of the nuclear reactor. Hence, the importance of understanding cryogenic flow boiling fluid physics should be highlighted in order to design high fidelity reactors and incorporated feed systems of NTP, akin to the critical role of understanding thermal hydraulics in pressurized water reactors (PWRs) for terrestrial nuclear reactors. Additional applications where CFM technologies play a critical role include, but are not limited to, ascent and descent stages, feedlines for gas/gas or liquid/liquid engines, and superconducting hydrogen aircraft.

1.2. Steady state heating experiments versus quenching experiments

Flow boiling experiments can be performed with two different methods: (a) *steady-state heating method*, and (b) *quenching (transient) method*. Described in Fig. 1(a), using the steady-state heating method, a boiling curve is generated by initiating experiments at zero power and increasing or decreasing wall heat flux in small increments, followed each by an adequate waiting period to allow wall temperature to reach steady state before it is measured. As wall heat flux is increased in small increments, Onset of Nucleate Boiling (ONB) point and Critical Heat Flux (CHF) are identified, delineating the nucleate boiling regime. Beyond the CHF point, further increase of wall heat flux allows for capture of the upper portion of the film boiling region. The second, *quenching* method assesses transient cooling performance by introducing colder liquid flow to preheated tube or channel, which, in turn, generates a complete temperature–time (quench) curve as shown in Fig. 1(b). It is important to note that the shape of the quench curve is strongly influenced by the thermal mass of the wall. Eventually, variation of the heat flux with wall superheat for each regime is determined via transient conduction analysis of the wall, generally using a lumped mass model.

Since the quenching method is inherently transient, recorded and analyzed data inherently includes transient uncertainties. Moreover, extracting HTC data from the quenching method requires the quantification of parasitic heat leak, introducing an additional potential source of uncertainty. In contrast, the heated tube method records data under steady-state conditions after the wall temperatures stabilize under fixed heat flux. Furthermore, since the imposed heat flux is generally one or two orders of magnitude higher than the parasitic heat leak, uncertainties are typically lower for the steady-state heating method compared to quenching experiments. Therefore, the steady-state heating method is preferred in flow boiling studies due to its greater accuracy in measuring heat transfer parameters of interest.

1.3. Previous cryogenic flow boiling experiments

As summarized in Table 1, numerous studies on cryogenic flow boiling, despite the inherent uncertainties, have predominantly utilized the quenching method to simulate the line-transfer and chilldown process during fuel transfer. In the 1960 s, represented by the studies of Burke et al. [5] and Brennan et al. [7], chilldown experiments were carried out using very long transfer lines but without flow visualization recordings. Instead, anticipated two-phase flow structures were inferred based on circumferential wall temperature measurements. Advancing to the 2000 s, chilldown experiments [8,9] with flow visualizations were carried out, confirming the prevalence of stratified flow during horizontal chilldown process. Subsequently, Hu et al. [12] conducted more comprehensive chilldown flow visualization experiments, systematically capturing flow patterns for both vertical upflow and vertical downflow configurations, and elucidated variations in chilldown heat transfer efficiency based on observed two-phase flow regime transitions during transient chilldown processes. More recently, in order to investigate the gravitational effects on heat transfer coefficients during chilldown processes microgravity quenching experiments were conducted. Kawanami et al. [10] conducted microgravity quenching

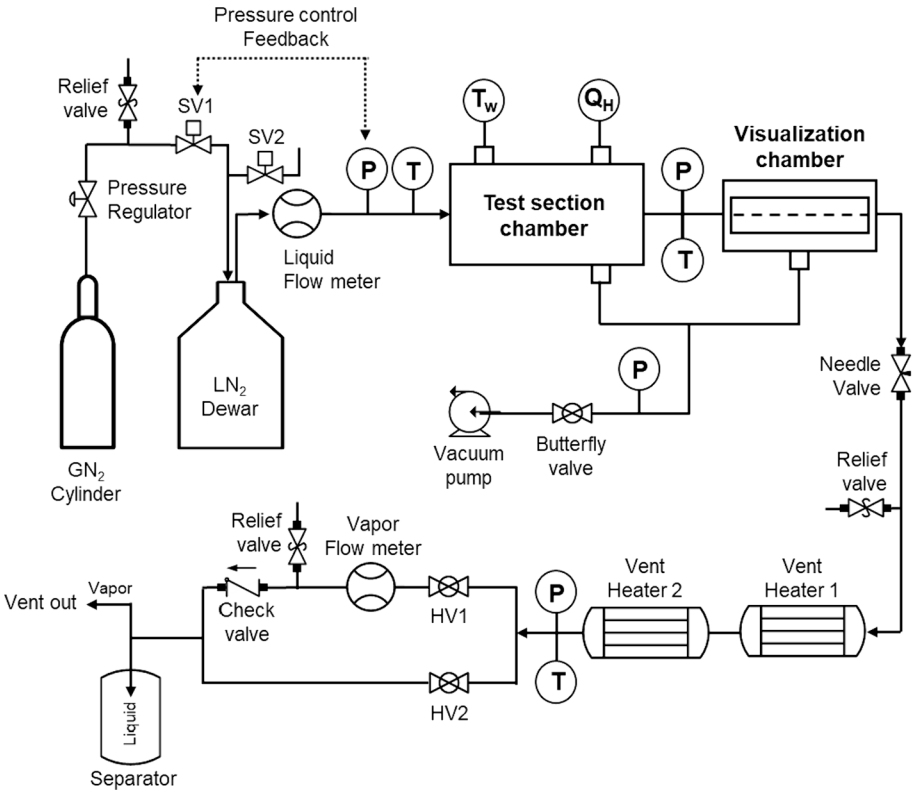

Fig. 2. Schematic of two-phase flow loop.

experiment using a 500-m drop tower which produced approximately 10 s of microgravity with levels of 10^{-4} to 10^{-3} of Earth's gravity and visualized the corresponding flow regimes. They explored the low G range of 300 to 500 kg/m^{2}s using vertically oriented transparent Pyrex glass tubes having an i.d. of 7 mm and a recorded flow length of 50 mm. They reported enhanced heat transfer coefficients in microgravity (μg_e) when compared to 1 g_e, reducing quenching time and increasing maximum heat flux during chilldown due to the increased quenching front velocity under μg. Yuan et al. [11] conducted microgravity quenching experiment using a drop tower which provided 1.7-s of microgravity with levels of 10^{-5} to 10^{-4} of Earth's gravity and visualized the corresponding flow regimes. They studied the very low G range of 3.6 to 10.8 kg/m^{2}s using a horizontally oriented transparent quartz tube having an i.d. of 11.1 mm and length of 254 mm. They observed degraded heat transfer in μg when compared to g_e and a slowed cooling rate of wall temperature during μg. Note that their data for μg was limited to the film boiling regime where flow regime is inverted annular flow. Darr et al. [15] conducted microgravity quenching experiment using parabolic flight on board a C9 aircraft which provided 20–23 s of μg. They covered the wider G range of 31 to 503 kg/m^{2}s using a stainless steel (SS304) tube with an i.d. of 11.68 mm and length of 572 mm. By comparing the microgravity quenching data to terrestrial gravity data, they found that the average heat flux for the reduced gravity test is 20–25 % smaller than that for 1 g_e and concluded that chilldown in reduced gravity environment is far less efficient than in any flow orientation in 1 g_e. As evidenced by the collective body of research on quenching methods, the study of quenching has not only expanded in terms of the number of investigations conducted but has also covered two-phase flow visualizations and the effect of gravity, two of which that are largely absent in cryogenic flow boiling experiments employing steady state heating method.

When it comes to steady state heating experiments, as summarized in Table 1, two important aspects of crogenic flow boiling are missing: flow visualization and microgravity experiments. First, the documentation of cryogenic two-phase flow visualization is notably scarce. Simoneau and Simon [18] presented a series of two-phase flow images, noting significantly greater vapor accumulation in vertical downflow compared to vertical upflow, and linked the observed flow structure to the lower CHF of vertical downflow. Several decades later, Fu et al. [25] reported microchannel flow patterns for LN_2 flow boiling in vertical upflow. Despite their efforts, the reported flow patterns, owing to the extremely small tube diameter, do not adequately represent macro-channel flow boiling of cryogens, which is pivotal for space applications where plumbing sizes typically exceed 6 mm. Second, the impact of reduced gravity on cryogenic flow boiling has never been investigated using the steady-state heating method. While continuous experimental efforts have been devoted to microgravity flow boiling for conventional fluids such as water or dielectric fluids by numerous researchers from the USA [27,28], Europe [29–31], Japan [32], and China [33], the exploration of cryogenic flow boiling in microgravity remains severely limited.

Accordingly, this gap in the database presents a significant challenge in the development of reliable and robust empirical correlations for heat transfer coefficients and critical heat flux in future cryogenic space applications. Consequently, it highlights the essential need for experimental investigations into cryogenic flow boiling, with specific attention to (a) utilizing steady-state heating methods, (b) acquiring systematic cryogenic two-phase flow visualization, and (c) obtaining cryogenic HTC and CHF data under reduced gravity conditions. As will be discussed in Section 1.4, the present study serves as a forerunner for upcoming parabolic flight experiments on uniformly heated cryogenic flow boiling.

1.4. Objective of present study

This study presents results obtained from cryogenic flow boiling experiments using LN_2 as the working fluid. The experiments are conducted under Earth's gravity in a horizontal flow orientation using a newly constructed cryogenic payload planned for upcoming parabolic

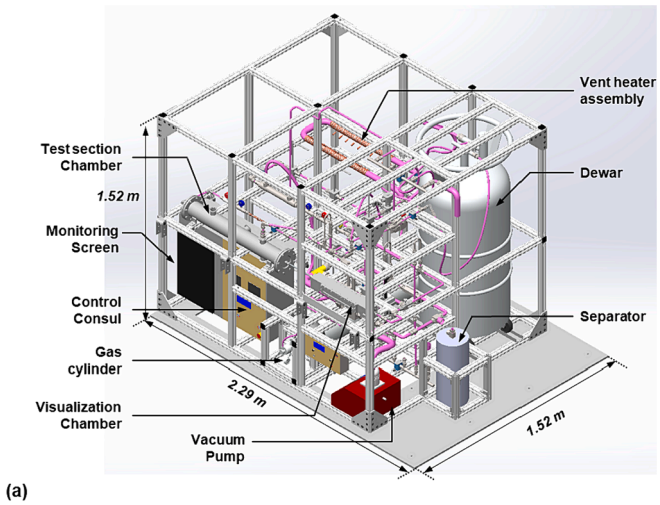

(a)

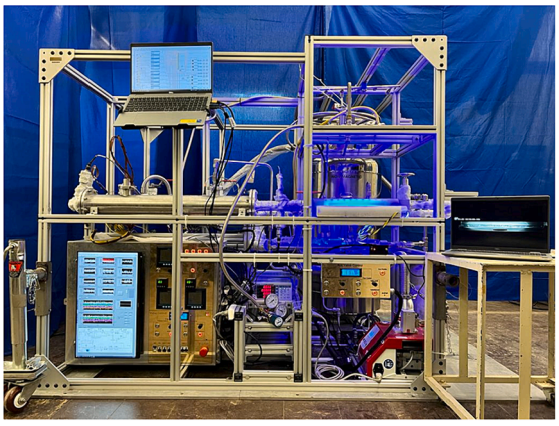

(b)

Fig. 3. (a) 3D CAD model and (b) picture of the experimental facility.

flight experiments. The overarching purpose of the experiments is to collect and acquire LN_2 two-phase heat transfer steady state data under terrestrial gravity for operating conditions which had been identified in [34] as gaps in previous databases. High-speed video flow visualization images are captured and presented to explain the two-phase flow physics along the heated tube for various operating conditions. Heat transfer results in the perspective of boiling curves, streamwise profiles of local wall temperature and local heat transfer coefficients, and averaged heat transfer coefficients are presented. Acquired experimental data are used to assess the accuracy of existing two-phase heat transfer correlations. In future studies, the present experimental data will be compared against the upcoming parabolic flight microgravity data to analyze the effects of different gravitational environments on two-phase heat transfer and fluid physics.

2. EXPERIMENTAL METHODS

2.1. Experiment facility

2.1.1. Two-phase flow loop

Fig. 2 shows a schematic of the open loop two-phase flow circuit utilized to provide working fluid, LN_2, into the inlet of the test section, and to safely vent outcoming fluid from the test section outlet to ambient air. Since the loop is designed to be an open circuit, a nitrogen gas cylinder with a volume of 44 L, which is initially pressurized up to 14.5 MPa, is connected to the LN2 dewar containing the bulk of the LN_2. By pressurizing the stored liquid in the dewar, the system builds up a positive pressure difference as a driving force to discharge liquid out of the dewar. At the outlet of the gas cylinder, as a primary safety measure, a pressure regulator equipped with an additional needle valve for fine control is installed to regulate the pressurization rate by controlling the gas flow rate. Between the pressure regulator and the dewar, a safety relief valve is installed to mitigate any uncontrolled pressurization accidents in case of the pressure regulator malfunctioning. The safety relief valve is set to open above 1585 kPa, depressurizing the system below the set pressure. The LN_2 dewar is a double-walled and vacuum insulated stainless steel tank which can store 160 L of LN_2 with an evaporation rate of 2.2 L per day. Since the experiment normally consumes 160 L within a day, the boil-off rate does not affect the performance of the system for this experiment. The dewar is double protected in terms of over-pressurization by installing both a safety relief valve and a burst disc. The safety relief valve is set at 1585 kPa which releases nitrogen gas out of the dewar when pressure exceeds the set pressure. However, to mitigate any potential failure of the safety relief valve, the burst disc, which is set for 2413 kPa, is directly attached to the same relief line eliminating the possibility of dewar explosion.

Powered by the pressure difference, liquid is pushed out of the dewar and flows into a turbine flow meter to measure flow rate. To convert measured volume flow rate into mass flow rate, fluid density information is required. Therefore, in order to accurately find the thermal properties of the incoming liquid, the temperature and pressure of the fluid are measured immediately after the flow meter. Fluid, then, enters the test section wherein a finite amount of heat is added to the fluid based on which the fluid phase changes and exits as two-phase mixture. At the outlet of the test section, a specially manufactured cross-shaped tube fitting is utilized to precisely measure outlet fluid temperature and pressure at the same axial location. Fluid then flows into the visualization chamber where fluid can be visualized through a transparent Pyrex tube. A high-speed camera is aligned with the visualization windows through which it captures two-phase flow regimes flowing through the transparent Pyrex tube. More design details for the test section and visualization chamber will be explained in Section. 2.2. A cryogenic grade needle valve is installed at the downstream of the visualization section to control the flow rate. The needle valve enables the fine tuning of mass velocity by sensitively controlling vertical movement of the needle in 11 rotations from full open to full close. Note that all the valves installed in the rig are certified for cryogenic temperature or used with U shaped candy cane tubes to prevent stem frosting issues. Two 3-kW rated vent heaters are serially connected at the downstream of the needle valve to fully evaporate any remaining two-phase mixture to pure vapor. At the outlet of the second vent heater, fluid temperature and pressure are measured which are coupled with volume flow rate reading from the vapor flow meter at the downstream of the vent heater to measure the mass flow rate.

The downstream portion of the flow loop is divided into two flowlines, one accommodating vapor flow meter and the other without a vapor flow meter. The opening of the flowlines is controlled manually using ball valves indicated as HV1 and HV2. The vapor flow meter is limited to measuring only low flow rates below $G = 100$ kg/m^{2}s. Any flow rate exceeding this mass velocity is measured with the liquid flow meter. When there is no need for the vapor flow meter, HV1 is closed to prevent failure of the turbine blade or bearing of the vapor flow meter due to abnormally high rotation speed. The two separate flowlines are merged and connected to a receiver tank which is installed to eliminate any possibility of liquid escaping outboard in improbable situations such as vent heater power loss. The two-phase mixture is then separated into liquid which is entrapped in the receiver tank and vapor escapes the tank and is vented out through vent ports.

Fig. 3 shows both a 3D CAD drawing and actual picture of the experimental rig containing all test components for eventual testing in the parabolic flight. The rig is built on an 12.7-mm thickness aluminum (AL7075-T6) baseplate with carved out hollow interior, and an 80/20 aluminum beam structure to fulfill structural integrity and weight restriction requirements simultaneously. The flow loop is situated in the

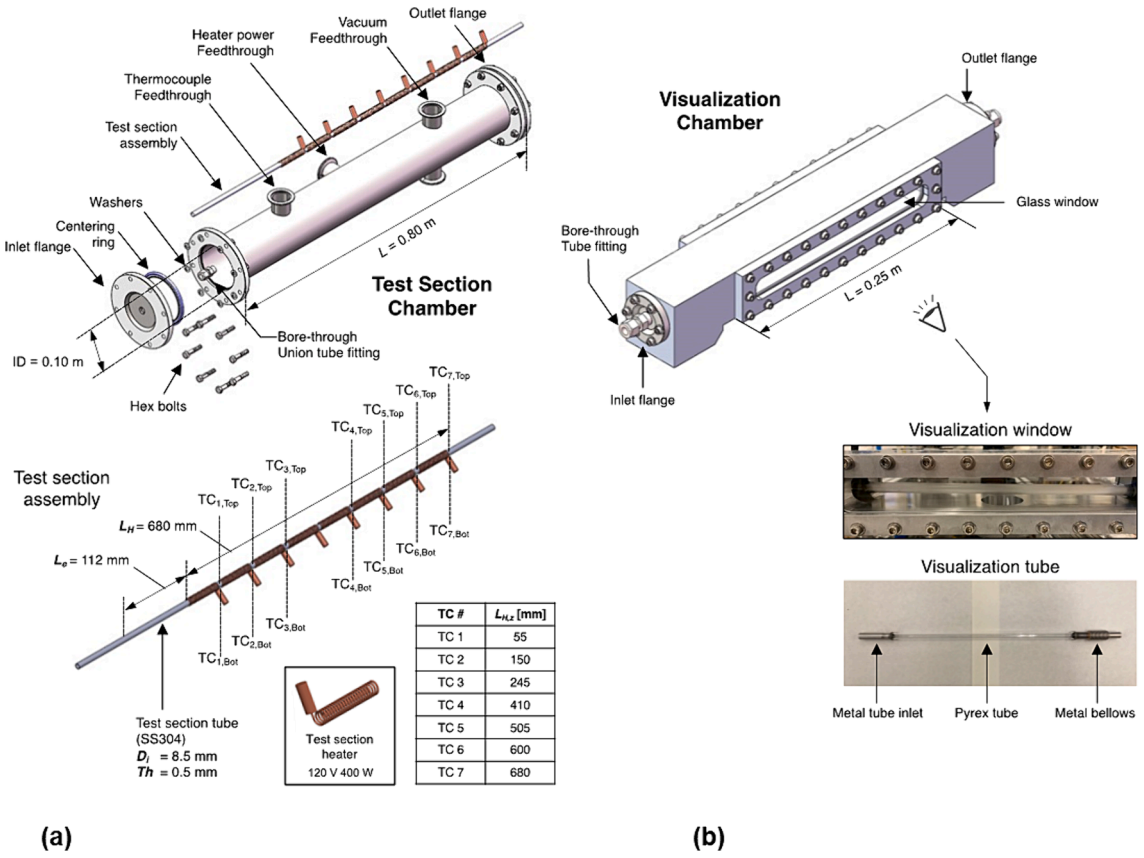

Fig. 4. Schematics of (a) test section chamber and assembly, and (b) visualization chamber with pictures of visualization window and Pyrex tube.

middle and lower planes of the rig. From the inlet of the test section to the inlet of the vent heater, the piping is maintained at the same elevation, preventing any secondary flow effects due to hydrostatic pressure differences. This is especially important for future parabolic flights in which gravitational acceleration drastically varies, and vertical movement of fluid can induce unwanted two-phase instabilities during flow boiling experiments. The dewar is mounted in the back-right cubicle with rails on which the dewar can be easily installed or removed. Two vacuum chambers, the test section chamber, and the visualization chamber, are positioned at the very front face of the rig, near to where system operators are situated. The vent heater assembly is stationed at the back left corner in the middle plane of the rig as a U-shaped tubing installed with 20 individual nozzle heaters producing 6 kW in total. All flow components, other than the receiver tank, are located inside the cuboid, leaving the receiver tank to be placed beneath the merged vent line for easy connection to a vent hose. The rig utilizes multiple gas vent hoses to discharge gas outboard the aircraft on flight or to ambient on the ground from various safety relief valves and a burst disc. On the bottom left corner of the rig, a control consul is situated. The control consul contains all electronical devices including a data logger, AC power distributors, a DC power converter, circuit breakers, heater power controllers for test section heaters, heater temperature controllers for vent heaters, power meters for each heater, and an Arduino board for pressure automation control. All the controlled and measured parameters are integrated through LABVIEW software and displayed through a monitor installed on the front face of control consul. Control and instrumentation will be discussed in detail in the later sections.

2.2. Test section and visualization section

The primary portion of the experimental facility is the combination of heat transfer test section, where the flow boiling takes place, and visualization section, where the flow is visualized. The test section is comprised of a test section chamber and a test section assembly as shown in Fig. 4. The test section chamber is a vacuum chamber in which the test section assembly is housed minimizing heat leak into the test section assembly by eliminating convective heat transfer from the surrounding air space. As shown in Fig. 4(a), the test section chamber has an inner diameter of 0.1 m and length of 0.8 m, having inner and outer flanges for both ends to ensure vacuum tight enclosing. Between the flanges, a centering rubber ring is placed to prevent air leak. The test section chamber is equipped with four feedthrough ports, three in vertical and one in horizontal. The horizontal feedthrough passes through heater power leads from eight individual test section heaters. The foremost vertical feedthrough passes thermocouple wires which are attached to the test section tube wall. Penetrated thermocouple wires are extended and fed into a control box at which the data logger is placed. Two vertical feedthroughs near the outlet are for vacuum hose connection. Either one can be used to connect the vacuum line, leaving the unused port to be capped close. All feedthrough ports are sized with the KF-40 flange standard. The test section assembly is comprised of a test section tube, eight individual test section heaters, and thermocouple wires. The test section tube is a thin wall ($Th = 0.5$ mm) stainless steel (SS304) tube with an inner diameter (D_i) of 8.5 mm, heated length (L_H) of 0.68 m, and entrance length (L_e) of 0.112 m. Note that the wall thickness was carefully selected based on the reported relation between CHF and wall thickness by Zhang et al. [35] which showed the independency of CHF with wall thickness thicker than 0.4 mm. To preserve the developed flow structure from the test section until the visualization section, the inner diameter is maintained constant with the inner diameter of test section tube from the inlet of the test section chamber to the outlet of the visualization chamber, minimizing any flow distortion. Eight individual electrically powered coil heaters, illustrated schematically in Fig. 4(a), are installed to provide uniform heat flux onto the test section tube wall.

Table 2
Measurement uncertainties.

Parameter	Error (%)
Fluid temperature, T_f	± 0.5℃
Wall temperature, T_w	± 0.5℃
Volume flow rate, $\dot{V}$	± 0.1 % reading
Absolute Pressure	± 0.25 % reading
Heat input, Q	± 0.25 % reading

Each individual heater is powered with 120 VAC, up to maximum power of 400 W, providing total of 3,200 W at full capacity. Each heater power lead is wired through relay switches to be separately powered while sharing a common voltage controller. Therefore, an operator can control all heaters with one controller and is also able to switch on and off each heater separately. A total of 14 thermocouple wires are attached on the tube wall at seven different axial locations having a top and bottom for each location. Details of the axial locations are provided as a table in Fig. 4(a). Note that the entire test section assembly is wrapped with two layers of insulation, first a layer with heater insulation and second an aluminum sheet layer, to minimize heat leak through convection and radiation heat transfer, respectively.

The visualization section is comprised of a visualization chamber and a visualization tube as shown in Fig. 4(b) with schematics of the chamber, and actual pictures of both. The visualization section chamber is a vacuum chamber in which the visualization tube is housed minimizing heat leak into the visualization tube by eliminating convective heat transfer from the surrounding air space. The chamber has rectangular stainless-steel housing with inlet and outlet flanges for both ends to ensure vacuum tight enclosing. Transparent glass windows are attached to each lateral side, providing a visualization length of 0.25 m. One side is viewed by the camera, and the other side is used for backlight illumination. The visualization tube is made of Pyrex glass with flexible metal bellows at one end, as shown in Fig. 4(b), to mitigate thermal stress on the glass. The tube has an outer diameter (D_o) of 9.5 mm with axially varying inner diameter due to glass manufacturing tolerance but is not very different from the inner diameter of the test section tube, which ensures the preservation of flow structure. The length of the visualization tube is longer than 0.25 m so that it can span the full window. Note that the analysis conducted with the captured flow images is unaffected by the refraction through the glass window and glass tube. The test section and visualization chambers are connected by adjoining the tubing which is then connected to a vacuum hose having a butterfly valve in between to isolate the vacuum line when needed. The vacuum hose is then directly connected to the vacuum pump. The vacuum pump is equipped both with a turbopump and a multistage diaphragm pump to achieve high to ultrahigh vacuum pressure. The pump used in the present facility is selected based on requirements to reach approximately 0.1 Pa within 15 min.

2.3. Instrumentation and Measurement accuracy

The flight rig is instrumented with three OMEGA type-E probe type thermocouples extending into the flow to measure local fluid temperature including test section inlet, test section outlet, and vent heater outlet. Local pressure measurements in the loop are made with four absolute pressure transducers from OMEGA, measuring four different locations along the two-phase flow loop including test section inlet, test section outlet, vent heater outlet, and vacuum pump inlet. As indicated in Fig. 4(a), a total of 14 type-E wire type thermocouples from OMEGA are installed on the tube surface to measure wall temperature along the test section tube. Two turbine flow meters are used to measure flow rate. The liquid flow meter measures liquid volume flow rates from $1.01\text{x}10^{-2}$ to $5\text{x}10^{-1}$ L/s. And the vapor flow meter provides vapor volume flow rate measurements from $9.4\text{x}10^{-1}$ to 7.1 L/s. Note that the measured volume flow rate is converted into mass flow rate using liquid or vapor density information acquired from temperature and pressure measurements very near to each flow meter. To power three different heaters including the test section heater, vent heater 1, and vent heater 2, three separate power ports are designed which exactly resemble the power system onboard the parabolic flight aircraft, obeying maximum allowable current requirements for the flight power supply system. Note that appropriately rated circuit breakers are installed for each power circuit to avoid any unintended power trip for flight power panels. The test section heater power, which is a major control parameter for the flow boiling experiments, is measured using Yokogawa WT310 high accuracy power meter. All temporal sensor output signals are collected and measured during the experiment using National Instruments data acquisition system (DAQ) at a sampling rate of 80 Hz. Collected temporal data are processed and are exhibited on the front monitor using LABVIEW software. Maximum uncertainties in the measurements of important parameters are given in Table 2.

2.4. Flow visualization

The dynamic interfacial behavior of the two-phase flow is visualized and recorded using a high-speed camera at each steady state point along the boiling curve and CHF. The transparent glass windows on each side of the visualization chamber and transparent Pyrex glass tube allow for excellent visual access to the adiabatic two-phase flow. Note that the flow is assumed to be adiabatic and its structure preserved from the outlet of the test section chamber until it is captured by video.

The high-speed camera is aimed at one transparent window while the opposite window is backlit with blue light emitting diodes (LEDs) for illumination. The backlight is diffused to provide uniform light intensity throughout the entire length of the visualization section using diffusing film. A Sentech high-speed camera is used which captures photographs of resolution 2040 (H) x 350 (V) pixels at a frame rate of 1000 frames/s and shutter speed of 25.8–45 μs. The captured images have a resolution of 2.85 pixels/mm. Each video image sequence consists of 250 frames, or 250 ms of flow visualization data per steady state point. It is noted that all high-speed video images reported in this paper have been uniformly post-processed to make the flow features more distinct.

2.5. Operating procedure

Since the two-phase flow loop is configured as an open loop system, maintaining the system pressure is one of the most important control factors during the operation. To control and to maintain system pressure, a high pressure nitrogen gas tank is used along with two solenoid valves for pressurization (SV1) and de-pressurization (SV2). The solenoid valves are automatically controlled by an automated control system using Arduino UNO. The automation code is configured to monitor the test section inlet pressure and to maintain the pressure to the set value. If the sensed test section inlet pressure is lower than the target pressure, SV1 opens for pressurization. Whereas if the sensed test section inlet pressure is higher than target pressure, SV2 opens for depressurization. However, with the nature of open loop system, if not pressurized, system pressure naturally decreases. After several preliminary testing runs, it is observed that sudden pressure reduction by opening SV2 is not necessary nor beneficial for system pressure control. Therefore, the automation code is amended to use only SV1 (the pressurization valve) to control system pressure.

To initiate the operation, the target system pressure is set as an input in the pressure control panel. Then, the liquid valve of the dewar is opened to allow liquid flow into the flow loop. Due to the sudden opening of the valve, system pressure drastically drops below the set pressure letting the automation system to start pressurization by opening SV1. The entire flow loop undergoes quenching with continuous fluid flow until the inlet condition is matched with target inlet subcooling and pressure. At the same time, it is always ensured that the fluid state is fully liquid by flow visualization monitoring. After the

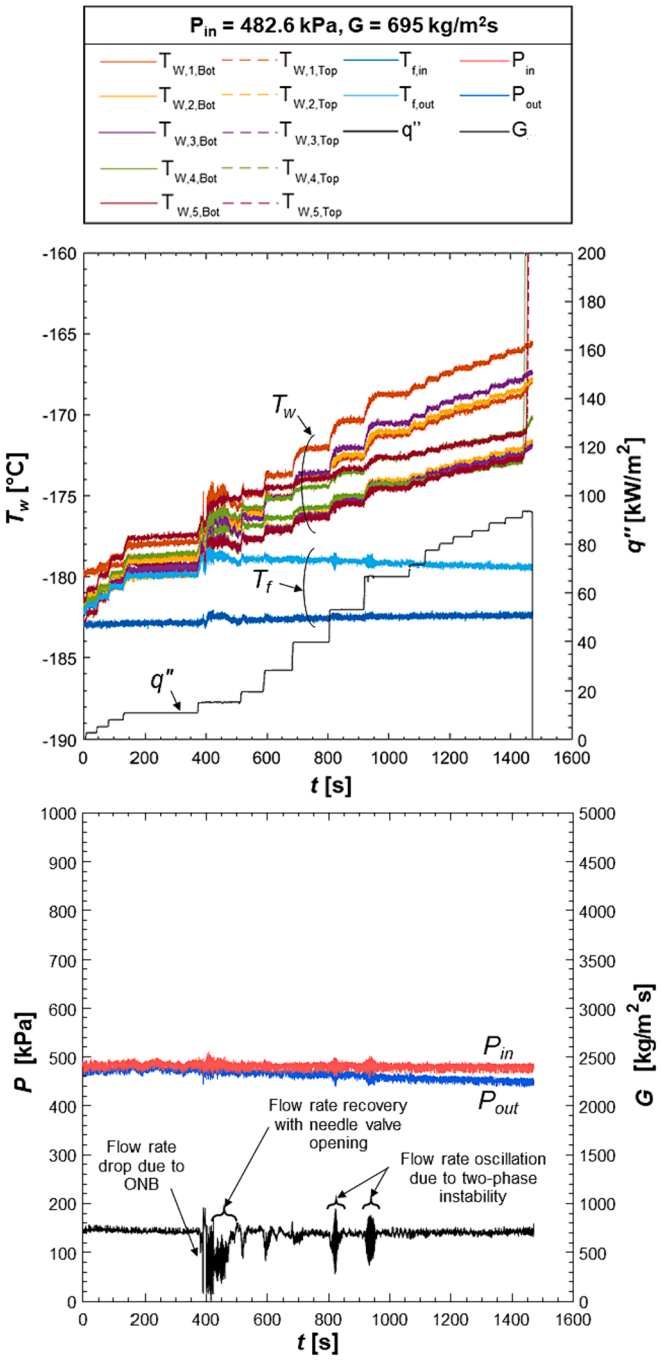

Fig. 5. Temporal variations of key system parameters in response to heat flux increments from zero to CHF for a set of operating conditions.

confirmation of a subcooled liquid state at the test section inlet, the needle valve is manually adjusted to match the flow rate to the target value. Note that both vent heaters are ensured to be powered on and automatically controlled by temperature controllers to maintain surface temperatures of 200°C whenever the fluid is flowing through the flow loop.

For each boiling curve, provided that the flow loop is fully quenched and has its inlet conditions matched, the test section heater is slowly powered up with small increments until CHF is reached. Note that with the increase of heater power, pressure drop across the test section increases due to increased vapor generation. Accordingly, due to the increased pressure drop, flow rate decreases, again, since the system is an open loop. Therefore, in order to maintain a consistent flow rate, the needle valve is manually operated to increase and match target flow rate for each boiling curve. After each heater increment, steady state is reached and maintained for steady state data recording and camera recordings. Subsequent analysis of the collected data confirms that a steady state is indeed reached for all heat flux increments. Although CHF is defined as the heat flux increment which causes an unsteady rise in surface temperature, for safety and simplicity, CHF is designated to have occurred at the heat flux increment which causes at least one of the wire thermocouples to show extreme temperature excursion. As CHF is reached, heater power is immediately ramped down to zero to prevent any damage to the test section or thermocouples. All temporal data and high-speed videos are recorded. This procedure is repeated for all predetermined inlet conditions in the test matrix.

2.6. Temporal temperature records for an entire boiling curve

Fig. 5 shows the temporal variations of recorded inlet fluid temperature, $T_{f,in}$, outlet fluid temperature, $T_{f,out}$, and heated wall temperatures, $T_{wi,Top}$ and $T_{wi,Bot}$, mass velocity, G, and outlet pressure, P_{out}, in response to incrementally increasing heat wall heat flux, $q"$, for the target operating conditions of inlet pressure of $P_{in} = 482.6$ kPa and $G = 695$ kg/m^{2}s. The temporal plots represent data corresponding to a representative boiling curve from $q" = 0$ to $q"_{CHF}$. For the initial four heater increments, until 380 s, due to the subcooled inlet condition, the flow remains as single-phase liquid without phase change. Starting from the fifth heater increment, the heat flux exceeds $q"_{ONB}$ causing wall temperature to overshoot but subside over time as nucleate boiling is established within the heated tube. With further increases in $q"$, nucleate boiling intensifies with wall temperatures attaining higher steady state values following each heat flux increment. Notice that the magnitude of $q"$ increments is reduced near CHF to capture the CHF point more precisely. At CHF, wall temperature shows unsteady excursions and, correspondingly, heater power is immediately turned down to zero power. During the entire test, T_{in} temperature is maintained constant, ensuring consistent inlet subcooling. Note that with the increasing pressure drop across the test section as heater power is increased, $T_{f,out}$ gradually decreases with time as more vapor is produced along the tube.

Fig. 5 also shows temporal variations of P_{in}, P_{out}, and G. With the aid of the automated pressure control system, P_{in} is maintained constant at the target pressure during the entire test, but P_{out} shows a gradual decrease with time due to increased vapor generation leading to an increased pressure drop. Note that the pressure control system employed in this experiment is designed with a rapid response time, enabling the maintenance of system pressure within ± 5 % of the targeted set pressure, not only for 1 g terrestrial ground operation but also for microgravity parabolic flight experiments. Notice the oscillations in G following each heater power increment. Especially at 380 s, when heat flux just exceeds $q"_{ONB}$, due to sudden emergence of bubbles and ensuing impact on pressure drop across the test section, G drastically oscillates since the flow loop is configured as an open loop system. As explained earlier, to maintain a constant mass velocity for each steady state point, the needle valve is manually adjusted after each heater power increment. As indicated in Fig. 5, the mass velocity recovers to the target value as the needle valve opens after each heater increment. It is important to note that the mass velocity conditions have been carefully maintained within ± 10 % boundaries of the targeted mass velocity conditions for each testing case.

Two-phase flow instabilities are encountered at higher heat flux conditions, as indicated by the oscillations in the pressures and flow rate, which fade away in a few seconds with further opening of the needle valve. The pressure and flow rate oscillations associated with these two-phase instabilities are distinct from events resulting from the heater increments, which are reflected by momentary decreases and fluctuations in flow rate but with no pressure oscillations. Note that such two-phase flow instabilities intensified at lower mass velocities than at higher.

Table 3
Summary of key parameters of the experimental study.

Parameter	Range
Mass velocity, G	406.76 – 1572.77 kg/m^{2}s
Mass flow rate,$\dot{m}$	0.023 – 0.089 kg/s
Inlet pressure,P_{in}	336.29 – 493.07 kPa
Inlet temperature, T_{in}	85.14 – 92.98 K
Inlet subcooling,ΔT_{sc}	0.57 – 4.35 ℃
Inlet quality,$x_{e,in}$	−0.05 – −0.01
Wall heat flux,q''_w	0 – 106.02 kW/m^2
Outlet quality,$x_{e,out}$	−0.05 – 0.26

2.7. Data processing and experimental ranges

Steady state data are extracted from recorded temporal data by identifying each heater increment and confirming wall temperature reaching steady state. Extracted temporal data are averaged for each steady state period. Necessary thermophysical properties for nitrogen are retrieved from NIST-REFPROP [36].

Test section inlet enthalpy is found based on measured P_{in} and $T_{f,in}$,

$$h_{in} = h(T_{in}, P_{in}) \tag{1}$$

Test section local enthalpy, h, at any z location from the heated inlet, and outlet enthalpy, h_{out}, are both calculated by application of energy conservation,

$$h(z) = h_{in} + \frac{q''\pi D_i z}{G\left(\pi D_i^2/4\right)} \tag{2a}$$

$$h_{out} = h_{in} + \frac{q''\pi D_i L_H}{G\left(\pi D_i^2/4\right)} \tag{2b}$$

Local thermodynamic equilibrium quality, $x_{e,z}$, is calculated according to the relation

$$x_{e,z} = \frac{h - h_f\big|_P}{h_{fg}\big|_P} \tag{3}$$

where h, h_f, and h_{fg} are, respectively, local z location values for enthalpy (from Eq.(2a)), saturated liquid enthalpy, and latent heat of vaporization corresponding to local pressure which is linearly interpolated between measured inlet pressure, P_{in} and outlet pressure, P_{out}.

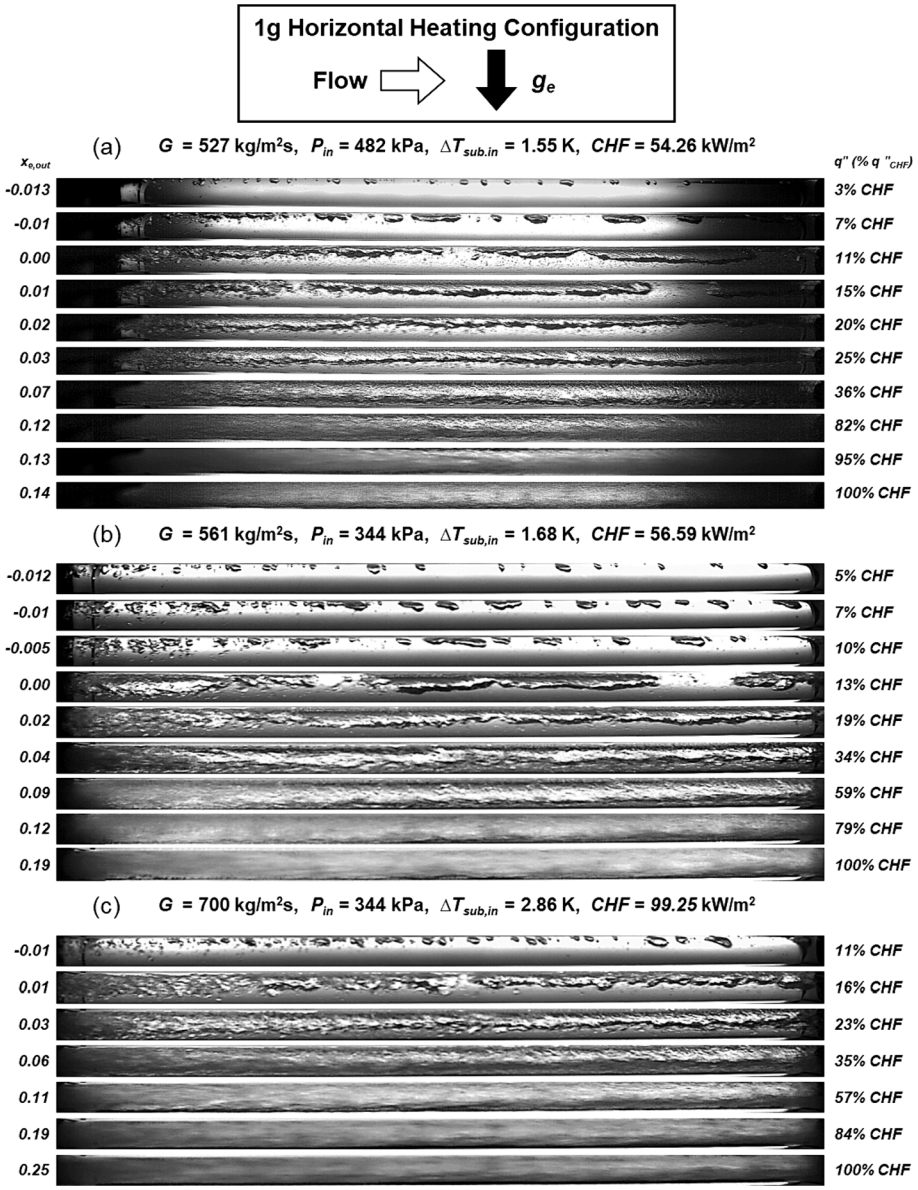

Fig. 6. Flow patterns along the boiling curve until CHF for near-saturated inlet at mass velocities of G = (a) 527, (b) 561, and (c) 700 kg/m^{2}s.

Local fluid temperature is determined based on the following relations:

$$T_{f,z} = \begin{cases} T_{in} + (T_{sat}|_{xe=0} - T_{in})Z/L_{sp} & x_{e,z} < 0 \\ T_{sat,z} & 0 \le x_{e,z} \le 1 \end{cases} \quad (4)$$

where L_{sp} is the heated single-phase length, which is calculated as

$$L_{sp} = \frac{G(\pi D_i^2/4)}{q''\pi D_i}(h_f|_{P_{in}} - h_{in}) \quad (5)$$

The local heat transfer coefficient (HTC) is defined based on measured local wall temperature and calculated local fluid temperature for each axial location,

$$h_z = \frac{q''}{(T_{w,z} - T_{f,z})} \quad (6)$$

Note that the wall temperature is measured along the outer surface of the heated tube. Therefore, the local inner wall temperature, $T_{w,z}$, is obtained from the measured outer wall temperature, $T_{w,o,z}$, by accounting for conduction resistance across the tube wall,

$$T_{w,z} = T_{w,o,z} - \frac{q''\pi D_i \ln(D_o/D_i)}{2\pi k_s} \quad (7)$$

where k_s is thermal conductivity of the tube wall. Notice that all q'' values in this study are based on the inner wall of the heated tube.

The average wall temperature is calculated using the relation

$$\overline{T}_{w,avg} = \frac{\iint T_{w,z}dA}{\iint dA} \quad (8)$$

The average heat transfer coefficient is calculated using the relation

$$\overline{h} = \frac{\iint dA}{\iint \frac{1}{h_z}dA} \quad (9)$$

which is based on harmonic averaging as proven by Ganesan et al. [34] for a constant wall heat flux boundary. Note that both Eq. (8) and Eq. (9) were performed for the entire test section length.

Ranges of operating conditions for the study are summarized in Table 3. Note that upcoming parabolic flight experiments will be conducted with similar operating parameter ranges to enable the direct assessment of the gravitational impact on flow boiling in tubes for cryogens.

3. FLOW VISUALIZATION RESULTS AND DISCUSSION

3.1. Flow visualization for low mass velocity

3.1.1. Flow patterns for low mass velocity

Recorded flow visualization results for three different operating conditions having relatively low mass velocities among the experimented test ranges are shown in Fig. 6(a)–(c). The flow direction is horizontal, from left to right, with vertically downward Earth gravity. As explained earlier in Section 2.2, all the presented flow pattern recordings are captured from the adiabatic visualization section which is located just downstream from the uniformly heated test section. Included for each operating condition are high-speed video images recorded at a steady state for heat flux increments from right above ONB until (and including) CHF. The wall heat flux, q'', indicated left of each image in a percentage of respective q''_{CHF} for the given operating conditions, as described in the following equation.

$$\%CHF = \frac{q''_{measured}}{q''_{CHF}} \times 100[\%] \quad (10)$$

Fig. 6(a) exhibits flow patterns along the boiling curve for operating conditions of $G = 527$ kg/m^{2}s, $P_{in} = 482$ kPa, and $\Delta T_{sub\ in} = 1.55$ K. For the heat flux of 3% q''_{CHF}, wall superheat surpasses required superheat for bubble nucleation evidenced by bubble formation along the heated test section. Due to the small surface tension of cryogens, nucleated bubbles easily detach from the heated wall despite their small size. Departed bubbles then migrate towards the top surface with the aid of the body force. The resulting flow pattern is bubbly flow having numerous small sized bubbles concentrated near the top surface. With a slight increase of heat flux up to 7% q''_{CHF}, the bubbles become larger due to higher wall superheat, activating a greater number of nucleation sites on the heated wall. Departed bubbles effectively coalesce each other while traveling, resulting in larger and longer bubbles, as captured in the recording. At 11% q''_{CHF}, aggressively nucleated and departed bubbles coalesce to form elongated vapor structures with an unstable wavy liquid–vapor interface flowing near the top wall, typical of plug flow. Notice numerous small grain-like bubbles flowing under the vapor structure that merge into the vapor stream atop. Further dialing up the heat flux up to 15% q''_{CHF}, vapor plugs are getting thicker due to an enhanced vapor production rate and coalescence to form even longer plugs. At 20%–25% q''_{CHF}, aggressive coalescence takes place to produce a continuous vapor film structure spanning almost the entire visualization section length, causing vapor stratification. However, note that the flow pattern is not perfect stratified flow having the top surface entirely covered by vapor film. Instead, the presented flow pattern shows a very thin layer of liquid persisting on top of the vapor structure. Due to high vapor velocity, liquid flowing under the vapor structure is dragged up and around the periphery, forming a thin layer of liquid fully wetting the tube. This flow pattern is called stratified annular flow as was identified and explained by Van Dresar and Siegwarth [37] whose experiments were focused on the lower mass velocity range rather than that of the current study. At a heat flux range of 36% q''_{CHF} to 82% q''_{CHF}, the annulus liquid layer becomes thinner and the vapor core grows thicker with increasing heat flux. As the vapor volume fraction increases, due to further fluid acceleration, flow stratification gradually fades away resulting in a relatively symmetric flow structure. Near CHF, at 95% q''_{CHF}, uniform annular liquid layer thickness can be observed along with a thicker and faster vapor core. At CHF, liquid layer thickness remarkably attenuates, especially near the top surface, increasing the chances of the top liquid layer being partially dried out. The partially dried out surface within the test section, which is then continuously exposed to a vapor-only environment lacking latent heat transfer, experiences a sudden increase of wall temperature excursion—in other words, CHF.

Fig. 6(b) portrays flow patterns along the boiling curve for operating conditions of $G = 561$ kg/m^{2}s, $P_{in} = 344$ kPa, and $\Delta T_{sub\ in} = 1.68$ K. Notice the more uniform backlight illumination for Fig. 6(b) and 6(c) when compared to Fig. 6(a) with additional backlight installation and upgraded light diffusion mechanisms. Similar flow regime transitions from the previous case can also be observed with clearer images. Having very similar operating conditions between Fig. 6(a) and Fig. 6(b), note that they both have almost the same q''_{CHF} values, proof of repeatability of the flow and heat transfer behaviors. From 5% to 9% q''_{CHF}, just surpassing q''_{ONB}, vapor bubbles are nucleated from the heated wall and depart to form discrete small bubbles near the top surface. With increasing heat flux, accumulated bubbles grow in size due to more efficient bubble coalescence. At 13% q''_{CHF} to 34% q''_{CHF}, an elongated vapor structure is produced and merges to span almost the entire length of the visualization section resulting in stratified annular flow. Notice how narrow is the heat flux range for the flow regime to transition from bubbly flow to annular flow. For cryogens having smaller latent heat of vaporization, h_{fg}, and surface tension, σ, when compared to those of room temperature fluids, bubble departure frequency is higher with smaller bubble size. Therefore, this leads to a decreased range of intermittent flow and an earlier transition to annular flow. At 59% q''_{CHF} until CHF, with increased fluid inertia due to flow acceleration, flow stratification attenuates, leading to the development of annular flow. Due to the low h_{fg}, the required wall superheat for cryogens is lower than that of room temperature fluids. This unique characteristic of cryogens enables persistent bubble nucleation even within annular liquid film

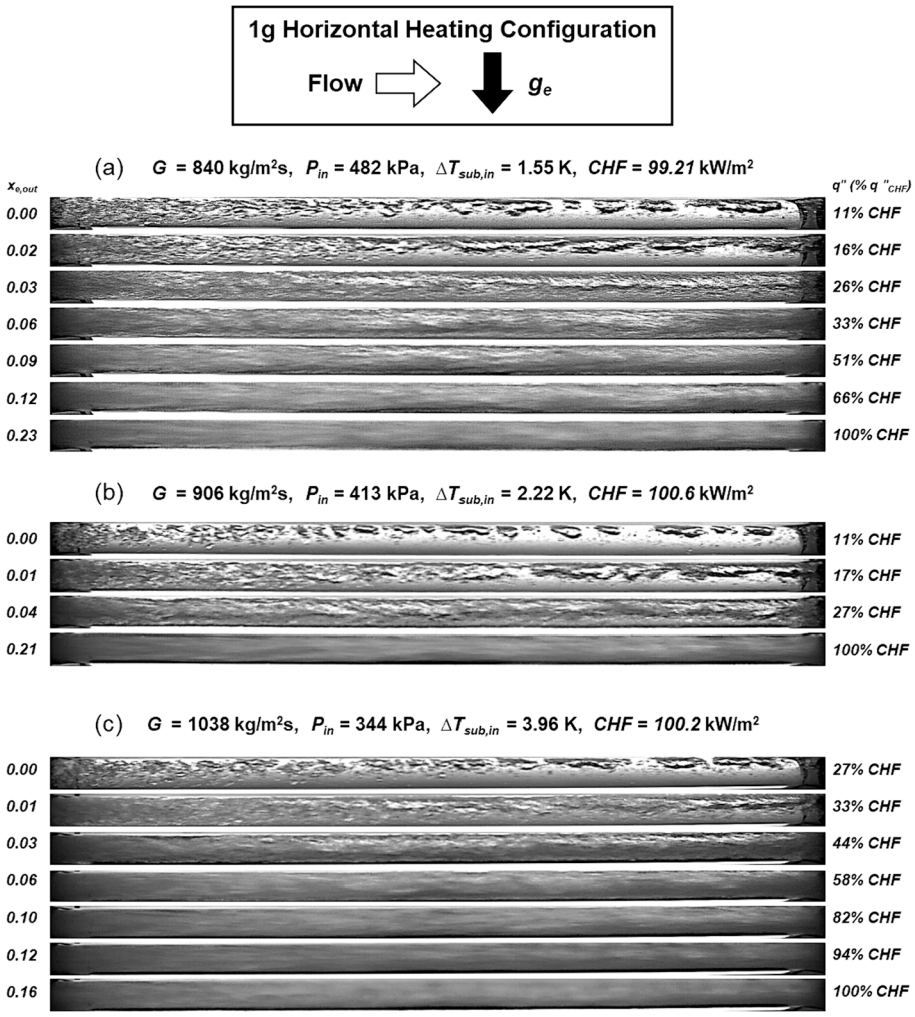

Fig. 7. Flow patterns along the boiling curve until CHF for near-saturated inlet at mass velocities of G = (a) 840, (b) 906, and (c) 1038 kg/m^{2}s.

which does not stop even at higher wall heat flux. Proving the suggested explanation, numerous small bubbles in the annular liquid film can be commonly observed in the heat flux range from 34% $q"_{CHF}$ until CHF in Fig. 6(b), where the flow patterns are annular. This persistent bubble nucleation in annular flow was predicted by Ganesan et al. [34,38] and also observed in recorded high-speed images acquired from chilldown experiments conducted by Baek et al. [39].

Fig. 6(c) depicts flow patterns along the boiling curve for operating conditions of $G = 700$ kg/m^{2}s, $P_{in} = 344$ kPa, and $\Delta T_{sub\ in} = 2.86$ K. Mass velocity is notably higher than the cases depicted in Fig. 6(a) and 6(b), yet a similar flow pattern progression until CHF is observed except for the following differences. With similar heat flux percentage, vapor bubble size is much smaller at higher mass velocity. For example, at 11% $q"_{CHF}$ in Fig. 6(c), one can see bubbly flow whereas at the same heat flux percentage in Fig. 6(a) plug flow with an elongated vapor structure can be seen. Similarly, at 13% $q"_{CHF}$ in Fig. 6(b), thick and continuous vapor plugs can be seen, but at 11% $q"_{CHF}$ in Fig. 6(c) the flow pattern is still bubbly with numerous discrete small bubbles. Due to higher flow inertia under the higher mass velocity condition, departed small bubbles are rapidly flushed away without having a chance to merge with neighboring bubbles to form larger vapor structures. Accordingly, at a higher mass velocity, it requires greater wall heat flux to reach annular flow. Notice the enhanced CHF value at higher G, almost double the CHF at lower G.

3.2. Flow visualization for high mass velocity

3.2.1. Flow patterns for high mass velocity

Recorded flow visualization results for three different operating conditions having relatively high mass velocities among the experimented test ranges are shown in Fig. 7(a)–(c). Fig. 7(a) exhibits flow patterns along the boiling curve for operating conditions of $G = 840$ kg/m^{2}s, $P_{in} = 482$ kPa, and $\Delta T_{sub\ in} = 1.55$ K. Due to the increased mass velocity, captured images of interfacial behaviors are not clear as in low mass velocity cases. At 11% and 16% $q"_{CHF}$, near the inlet of the visualization section, a great number of small bubbles are observed in a well distributed manner across the tube diameter. Here, with the increased inertia at high G, the dominancy of body force is attenuated than at low G, showing a uniform distribution of small vapor bubbles. Also, notice the shape of the bubbles is laterally squeezed due to the combined effects of inertia and buoyancy. As explained earlier, due to the reduced mixing and turbulent effects with the absence of boiling inside the visualization tube, the small bubbles from the inlet merge to form a larger bubble as they flow along the visualization tube. Due to the enlarged vapor volume for the merged bubbles which are more susceptible to buoyancy force, they tend to skew toward the upper portion of the tube. At 26% and 33% $q"_{CHF}$, with the increased vapor velocity due to the increased vapor generation under higher wall heat flux, an annular flow regime is observed. Affected by gravitational body force, the flow tends to thin the liquid film on the top portion of the tube wall and thicken it at the bottom. With further increases of heat flux, from 33% to 100% $q"_{CHF}$,

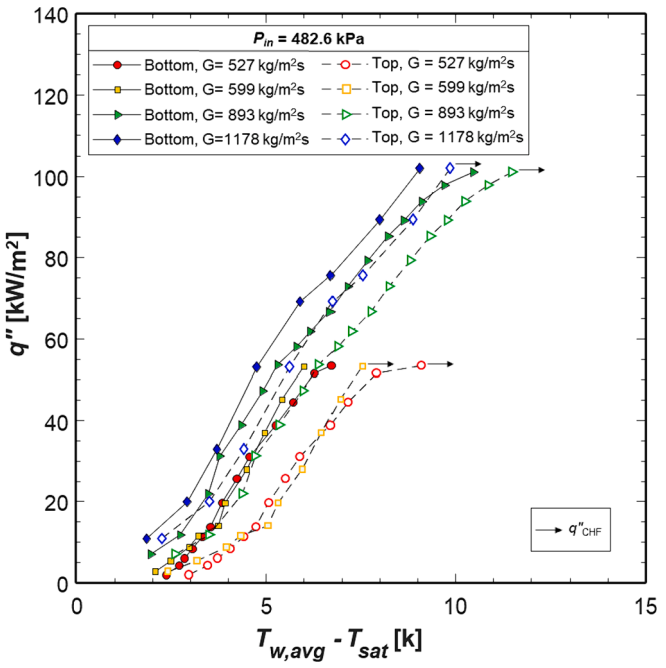

Fig. 8. Boiling curves at inlet pressure of 482.6 kPa illustrating effect of mass velocities for both bottom and top surfaces.

flow is further accelerated, increasing vapor velocities. Under sufficiently high vapor velocity, vapor flow is invariably turbulent causing liquid to be evenly distributed around the tube perimeter, against the tendency of gravity to stratify the flow.

Fig. 7(b) shows flow patterns along the boiling curve for operating conditions of G = 906 kg/m^{2}s, P_{in} = 413 kPa, and $\Delta T_{sub\ in}$ = 2.22 K. Having a higher mass velocity condition, which provided more liquid at the inlet under a similar heat flux condition, a lesser fraction of vapor volume is observed in Fig. 7(b) than in Fig. 7(a). For example, at the same 11% $q"_{CHF}$, bubble size is much smaller and the plug length is shorter at higher G, due to an increased inertia effect. Nevertheless, flow patterns near or at CHF in both cases are those of annular flow with thin liquid annular film and vapor at the core.

Fig. 7(c) shows flow patterns along the boiling curve for operating conditions of G = 1038 kg/m^{2}s, P_{in} = 344 kPa, and $\Delta T_{sub\ in}$ = 3.96 K. Notice the CHF value is almost constant regardless of the magnitude of mass velocities from Fig. 7(a) to 7(c). Even in the highest mass velocity condition, similar flow patterns and regime transitions continue but at higher heat flux percentages due to rapid vapor removal, which effectively disturbs bubble coalescence when compared to lower mass velocity conditions. For example, at 27% $q"_{CHF}$ in Fig. 7(c), a bubbly flow regime is observed while at 27% $q"_{CHF}$ in Fig. 7(b) and 26% $q"_{CHF}$ in Fig. 7(a), stratified annular flow is observed. Nevertheless, flow patterns near or at CHF in all the cases are patterns of annular flow with thin liquid annular film and vapor at the core. Notice the gradual thinning of both the bottom and top liquid layer thickness with heat flux percentage from 44% to 100% $q"_{CHF}$ based on which CHF is triggered by partial dry out of either top or bottom liquid film.

4. HEAT TRANSFER RESULTS AND DISCUSSION

4.1. Flow boiling curves

Boiling curves are an excellent way to show the heat transfer performance of a two-phase thermal management system. Fig. 8 shows a boiling curve for four different operating conditions having a mass velocity range of G = 527–1178 kg/m^{2}s and the same inlet pressure of P_{in} = 482.6 kPa for near-saturated inlet conditions. The boiling curve is plotted as wall heat flux against average wall superheat, which is defined as average wall temperature, $T_{w,avg}$, minus saturation temperature, T_{sat}. The figure includes both top tube and bottom tube curves to show the gravitational body force effect on boiling curves. All curves show common trends, beginning with increasing slope as the flow transitions from single-phase heat transfer to nucleate boiling, then they continue with the increased slope which ends with a reduction just before CHF. Note that points where the slope increases in the low heat flux region do not necessarily refer to ONB since the local wall temperatures are averaged to represent the entire test section. However, the transitions mark the starting points of the dominancy of latent heat transfer over single-phase forced convective heat transfer. The nucleate boiling region, the most favorable two-phase flow regime in various industrial applications, carries over a wide range of heat flux as depicted in the boiling curves showing relatively modest increases in the wall temperature. As explained in Section 3.1.1, for cryogens, due to the lower required wall superheat for bubble nucleation, the suppression of nucleate boiling is dampened, and nucleate boiling persists in annular flow which generally appears in high heat flux conditions. As the annular liquid film gets thinned with further increases of wall heat flux almost reaching CHF, due to the unstable liquid–vapor interface, intermittent dryout occurs, exposing the heated wall to vapor-only environment. With insufficient liquid replenishment to the heated wall, the wall temperature increases without stabilizing, which indicates CHF. In Fig. 8, the effect of increasing mass velocities on flow boiling can also be observed. First, as indicated with arrows, with the increase of mass velocity, $q"_{CHF}$ increases dramatically. However, the increase is not linearly proportional to the increase of mass velocity but stagnates at a certain threshold. Second, with increasing mass velocity, the entire boiling curve shifts upwards both for the top and bottom curve sets. This indicates that high G flow can sustain nucleate boiling for larger heat fluxes due to more efficient vapor removal with the higher fluid inertia followed by liquid replenishment for more nucleate boiling. Third, with the increase of mass velocity, the top and bottom curves at each operating condition become closer to each other, indicating a smaller wall superheat difference between the bottom and top surfaces. As shown from the flow visualization in Section 3.2, at high mass velocity, flow stratification attenuates with a more uniform distribution of liquid due to invariably turbulent vapor flow at high vapor velocities. Therefore, with less stratification, more uniform radial profile of wall temperature can be achieved which reduces the wall superheat difference between the bottom and top surfaces of the heated tube.

4.2. Local measurements

4.2.1. Local wall temperatures

Streamwise local wall temperature ($T_{w,z}$) profiles for different heat fluxes are presented in Fig. 9(a)–(d) at a mass velocity range of G = 527–1178 kg/m^{2}s under the same inlet pressure condition of 482.6 kPa. Within each plot are included $T_{w,z}$ profiles for three different heat fluxes ranging from ~ 10% $q"_{CHF}$ to the heat flux increment preceding CHF. At all operating conditions, the T_w at each streamwise location monotonically increases with increasing heat flux. In all of the cases, the streamwise profile is relatively flat without a dramatic increase or decrease of wall temperature, implying a highly nucleate boiling dominant flow regime in the test section throughout the given operating conditions. Due to the gravitational body force effect, the top wall temperature is always higher than the bottom wall temperature in all of the operating conditions. The gap between the top and bottom temperatures increases with the increase of wall heat flux since a larger vapor structure is formed and accumulated near the top surface at higher $q"$. Note that the initial decrease of the bottom wall temperature near the inlet is due to axial conduction from the test section chamber flange.

At low mass velocity conditions, as shown in Fig. 9(a) and 9(b), regardless of the provided wall heat flux, bottom streamwise profiles for bottom surface temperatures remain almost constant. This trend agrees

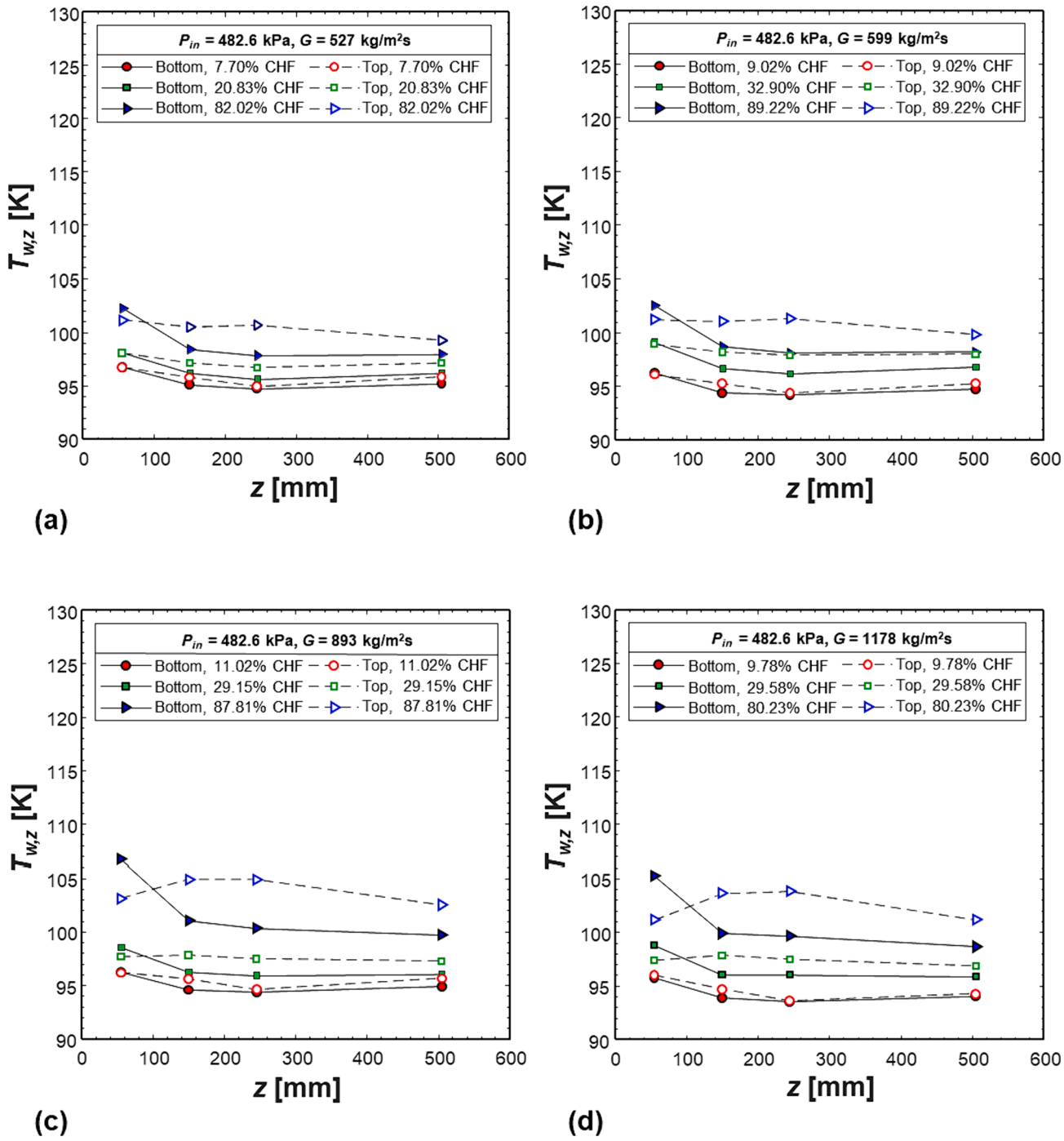

Fig. 9. Streamwise local wall temperature profiles under different heat fluxes for four different mass velocities of G = (a) 527, (b) 599, (c) 893, and (d) 1178 kg/m^{2}s at the same inlet pressure of 482.6 kPa.

with the flow visualization observation in Section 3.1, having the bottom surface always in contact with bulk liquid which accommodates active bubble nucleation and bubble departure, enabling effective heat diffusion and preventing significant increases of wall temperature. The explained bottom wall temperature behavior highlights the advantages of the nucleate boiling regime in two-phase cooling systems in that the system cannot only maintain sound temperature but also provide uniform temperature distribution which will benefit applications where uniform temperature is required. For the top surface at low mass velocities, with increasing heat flux, streamwise profiles point slightly upward and are concave, having local T_w maxima at $z = 245$ mm. The T_w for the top surface at the upstream region from the test section inlet to the local maxima shows a slight increase as the flow regime progresses to annular flow. Whereas after the local maxima, at farther axial locations near to the test section outlet, T_w decreases. As the vapor volume fraction increases with the axial location, flow at the downstream is accelerated due to the increased specific volume. This increased flow velocity in turn helps in more cooling of the wall due to increased turbulence and fluid mixing. Therefore, these flow acceleration effects override the effects of heat addition, and eventually decrease wall temperature. In high mass velocity cases in Fig. 9(c) and 9(d), similar streamwise wall temperature trends are presented with intensified upward concavity at the top surface having local T_w maxima between $z = 150$ mm and 245 mm at high heat flux conditions.

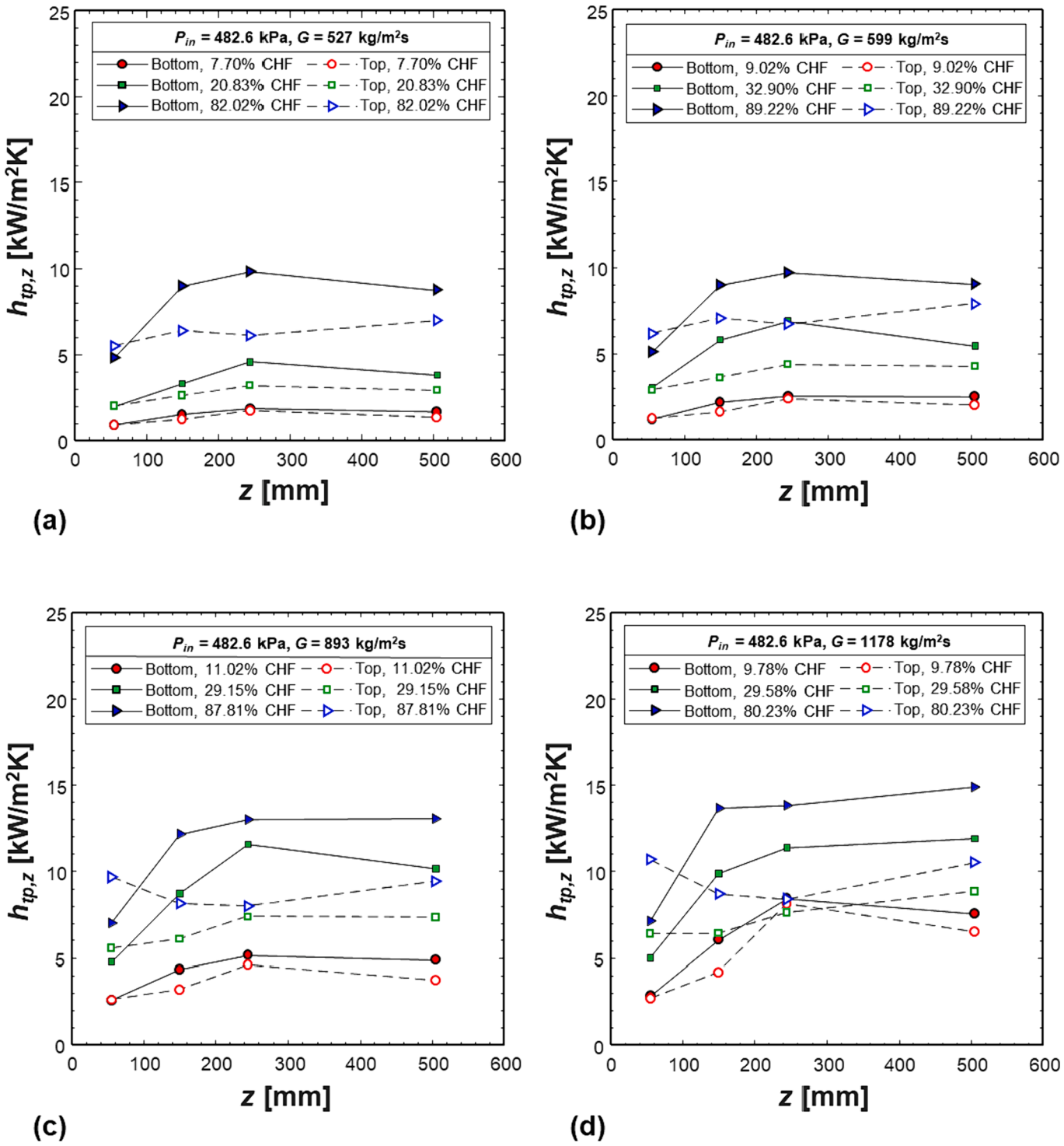

Fig. 10. Streamwise local heat transfer coefficient profiles under different heat fluxes for four different mass velocities of G = (a) 527, (b) 599, (c) 893, and (d) 1178 kg/m^{2}s at the same inlet pressure of 482.6 kPa.

4.2.2. Local heat transfer coefficients

Streamwise local heat transfer coefficient (h_{tp}) profiles for different heat fluxes are presented in Fig. 10(a)–(d) for a mass velocity range of G = 527–1178 kg/m^{2}s under the same inlet pressure condition of 482.6 kPa. The overall layout of Fig. 10 and the operating conditions of each sub-plot are exactly the same as Fig. 9. To understand local flow and heat transfer physics from horizontally oriented flow boiling results, it is convenient to start with the bottom surface first. At all operating conditions, local heat transfer coefficient profiles for the bottom surface monotonically increase in magnitude with increasing wall heat flux. In Fig. 10(a) and 10(b), at the lowest heat flux condition wherein active nucleate boiling takes place throughout the test section, the local h_{tp} profile shows a slight increase from the inlet to the middle of the test section due to the intensification of boiling with increasing wall superheat. For the remaining part of the test section, the profile maintains magnitude by accommodating an effective boiling cycle commencing from bubble nucleation, then to bubble growth, and finally to bubble departure which, in turn, refreshes hot surfaces with cold bulk liquid

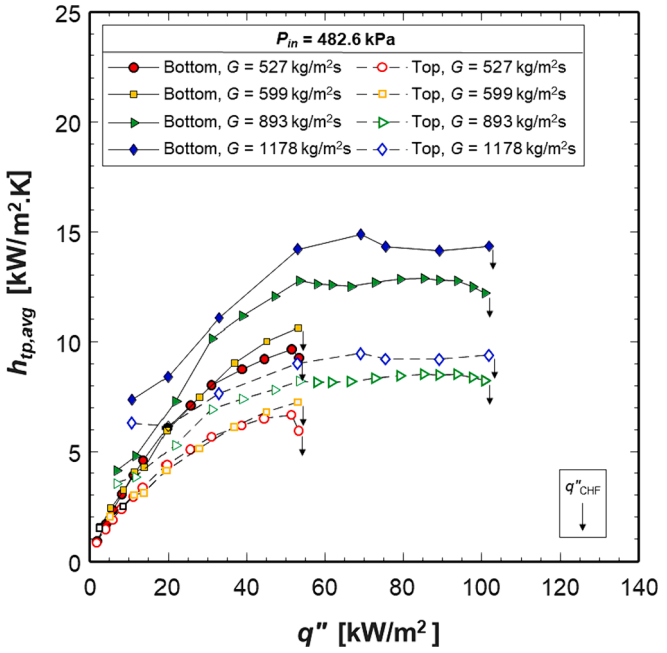

Fig. 11. Average heat transfer coefficient variation at inlet pressure of 482.6 kPa illustrating effect of mass velocities for both bottom and top surfaces.

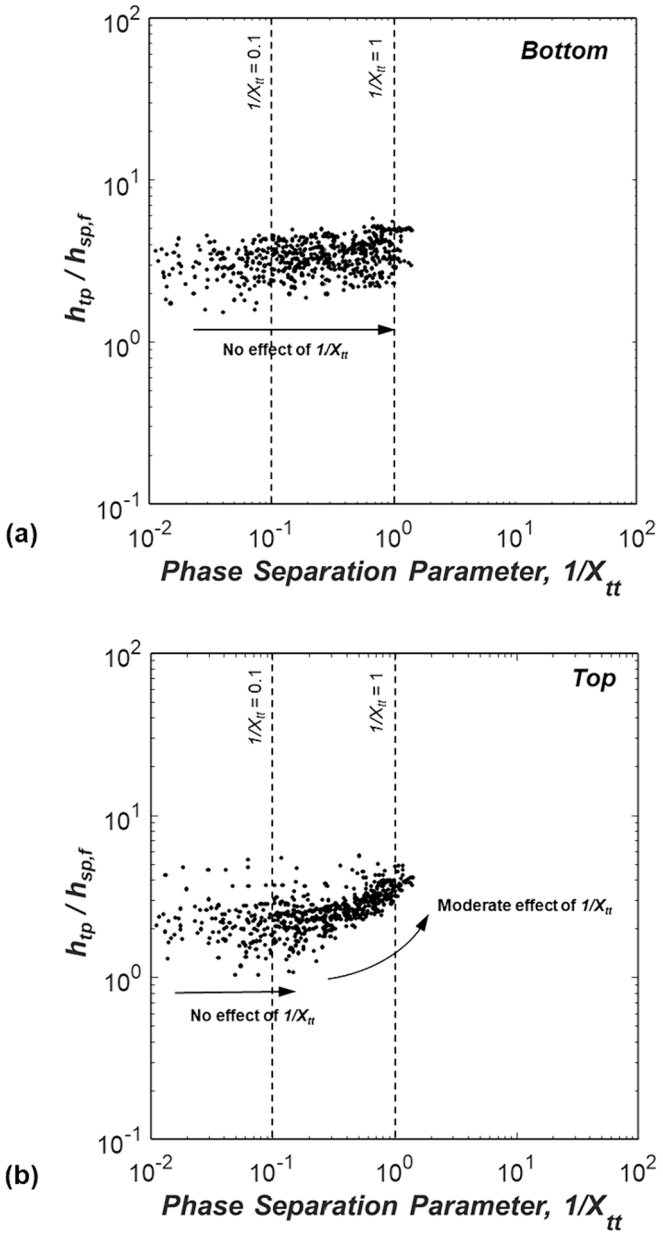

Fig. 12. Variation of h_{tp}/h_{sp} with phase separation parameter $1/X_{tt}$ for (a) bottom surface and (b) top surface.

helping another boiling cycle to start. At higher heat flux conditions, the streamwise h_{tp} profile shows a larger slope of increase due to enhanced nucleate boiling with increased heat flux activating a greater number of cavities, resulting in more aggressive bubble nucleation and departure which can also be seen from the flow visualizations of earlier sections. At farther axial locations under the same heat flux, due to bubble crowding and coalescence, bulk liquid supply to the heated wall is disturbed which in turn drags down the heat transfer coefficient. At the highest heat flux in both plots, streamwise h_{tp} shows relatively flat profiles, which are high in magnitude. For low mass velocities, as indicated in Fig. 10(a) and 10(b) near CHF, the flow regime is annular but with asymmetrical annular film thickness having the bottom layer thicker than the top layer. Therefore, within the thick bottom liquid annular layer, nucleate boiling sustains and aids in effective heat diffusion by actively nucleating bubbles, consuming heat load for vaporizing latent heat. Similar streamwise behavior for bottom surface h_{tp} is observed in Fig. 10(c) and 10(d), but with larger slopes of the profiles. Due to the increased flow inertia, the generated vapor structures on the bottom surface are effectively flushed and refurbished with bulk liquid. In addition, increased inertia aids in more aggressive mixing and turbulence within the fluid which not only retains nucleate boiling but also increases the heat transfer coefficient. Note that the CHF value for each percentage is different for each plot. For Fig. 10(c) and 10(d), CHF values are much higher than those with lower G, as in Fig. 10(a) and 10(b). Due to the enhanced heat transfer performance with higher mass velocities, much higher heat load can be transferred and diffused by the two-phase boiling system without excursing wall temperature.

At all operating conditions, due to larger vapor accumulation near the top surface which degrades effective heat transfer from the heated surface to the fluid, top wall heat transfer coefficients are always lower than those of the bottom surface. As heat flux increases, the difference between the top and bottom increases with the coalescence of vapor bubbles constructing a voluminous vapor structure covering the top surface and effectively insulating the top wall from the bulk liquid. From Fig. 10(a)– 10(c), the local heat transfer coefficient profiles for the top surface reveal a monotonically increasing trend with an increase of wall heat flux, indicating the dependency of the heat transfer coefficient on heat flux. However, in Fig. 10(d) with the highest mass velocity condition, the heat transfer coefficient profile shows a different trend in the upstream and downstream. At the upstream, near the test section inlet, the local heat transfer coefficients increase, indicating a nucleate boiling dominant heat transfer regime. In comparison, from the middle to the downstream of the test section, increments of local heat transfer with increasing heat flux are far smaller, showing less or no dependency on heat flux indicating a declined dominancy of nucleate boiling.

4.3. Parametric trends on cryogenic heat transfer coefficients

4.3.1. Effect of heat flux and mass velocity

In Fig. 11, average heat transfer coefficient variations with wall heat flux are included for four different mass velocity conditions of $G = 527$, 599, 893, and 1178 kg/m²s under the same inlet pressure of 482.6 kPa for near-saturated inlet conditions. Both bottom and top curves are included in the same plot to understand the gravitational effects on the average heat transfer coefficient. In general, heat transfer coefficients at all operating conditions increase sharply at first with increasing heat flux and the increment gradually dwindles as heat flux increases. At each

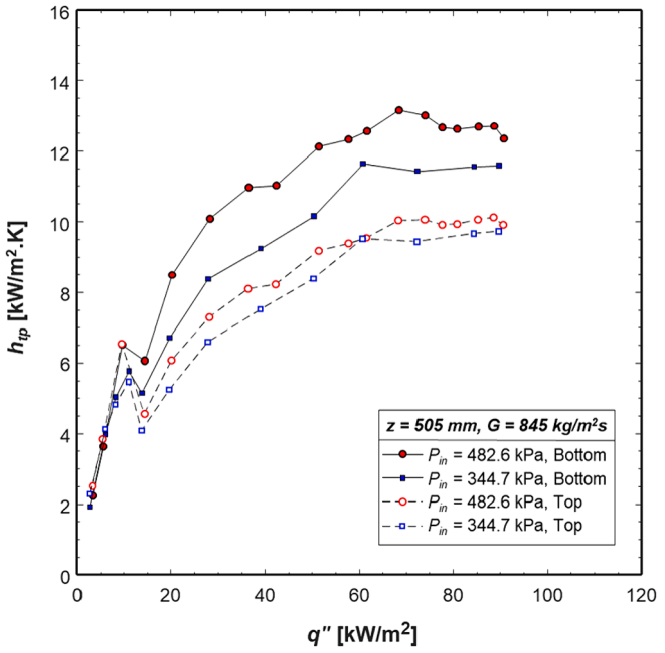

Fig. 13. Variation of local heat transfer coefficient with heat flux at axial location of $z = 505$ mm for mass velocity of 845 kg/m^{2}s under two different inlet pressures.

Table 4
Evaluation results of seminal flow and pool boiling HTC correlations against the measured HTC database.

Authors	Year	MAE [%] (Bottom)	MAE [%] (Top)	Functional form
Forster & Zuber[a] [43]	1955	12.37	50.67	$h_{tp} = h_{pb}$
Chen[b] [40]	1966	16.21	66.22	$h_{tp} = S.h_{pb} + F.h_{cb}$
Cooper[a] [44]	1984	19.99	64.84	$h_{tp} = h_{pb}$
Shah[b] [45]	1984	22.35	76.54	$h_{tp} = \max\{h_{nb},\ h_{cb}\}$
Gungor & Winterton[b] [46]	1987	33.25	92.94	$h_{tp} = h_{nb} + F.h_{cb}$
Klimenko[c] [47]	1990	16.27	58.63	$h_{tp} = \max\{h_{nb},\ h_{cb}\}$
Liu & Winterton[b] [48]	1991	13.64	37.81	$h_{tp} = S.h_{pb} + F.h_{cb}$
Steiner & Taborek[b,c] [49]	1992	12.21	48.02	$h_{tp}^{\ 3} = h_{nb}^{\ 3} + h_{cb}^{\ 3}$
Kim & Mudawar[b] [50]	2013	19.43	48.13	$h_{tp}^{\ 2} = h_{nb}^{\ 2} + h_{cb}^{\ 2}$
Ganesan et al.[c] [34]	2021	17.47	38.39	$h_{tp}^{\ 2} = h_{nb}^{\ 2} + h_{cb}^{\ 2}$

a Pool boiling correlation
b Flow boiling correlation based on data for different fluid types.
c Flow boiling correlation derived specifically for cryogenic fluids.

end of the curve, arrows are added to indicate CHF where a drastic decrease of heat transfer coefficient occurs due to sudden wall temperature excursion in the test section.

Flow boiling HTC correlations are often formulated in terms of two primary contributors to the heat transfer process: *nucleate boiling* and

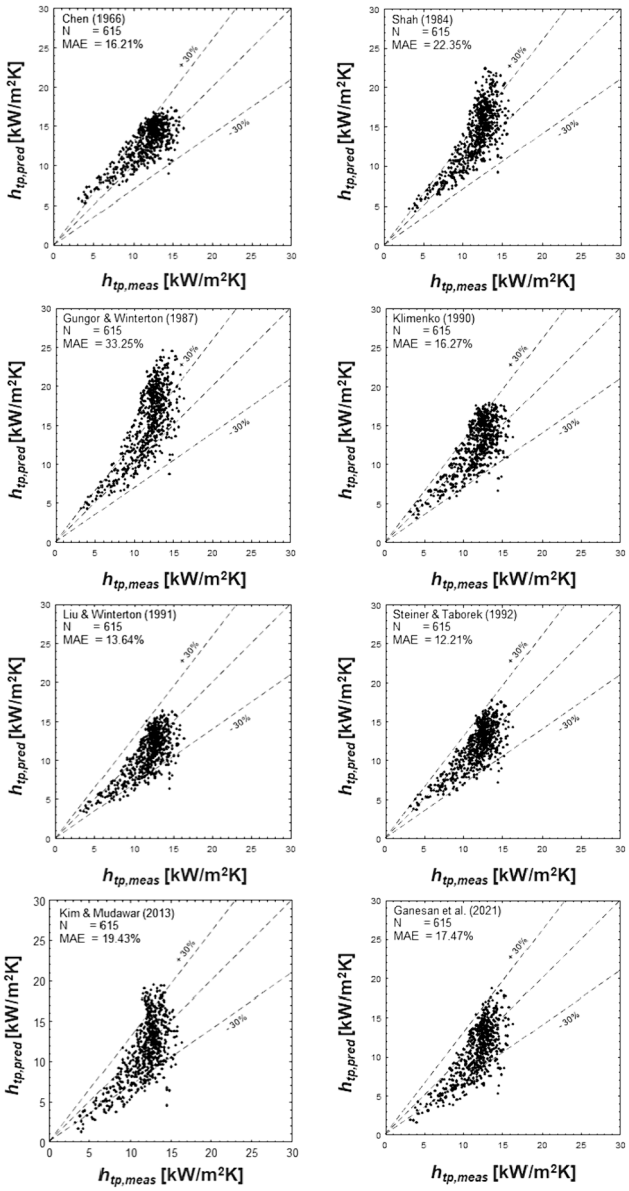

Fig. 14. Performance of seminal flow boiling HTC correlations against measured bottom wall HTC data.

convective boiling. As discussed in a later section, the HTC is therefore expressed as

$$h_{tp} = f(h_{nb}, h_{cb}) \tag{11}$$

where h_{nb} and h_{cb} are the heat transfer coefficients associated with nucleate boiling and convective boiling, respectively. Overall, the strength of contribution of h_{nb} or h_{cb} *to* h_{tp} is highly dependent on the operating conditions.

For low mass velocities, $G = 527$ and 599 kg/m^{2}s, the average heat transfer coefficient curves overlap on each other at low heat fluxes, showing a lesser dependency of latent heat transfer on fluid flow rate. Both curves commonly depict a steep increase of $h_{tp,avg}$ with increasing heat flux which signifies a large contribution of nucleate boiling. Here, at low mass velocities, soon after the deviation of $h_{tp,avg}$ curves from the nucleate boiling regime, due to the small thickness of annular liquid film on the top surface with weak flow inertia, a partial dryout of liquid film happens and triggers CHF. For high mass velocities, $G = 893$ and 1178 kg/m^{2}s, the average heat transfer coefficient increases sharply showing higher peak values than with lower mass velocities, which is then

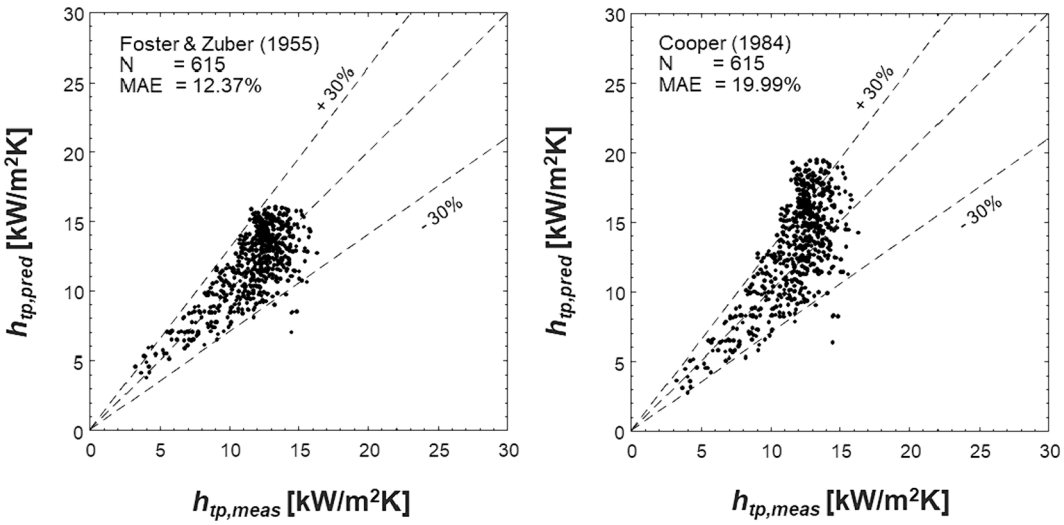

Fig. 15. Performance of seminal pool boiling HTC correlations against measured HTC data.

followed by an almost constant and large $h_{tp,avg}$ until CHF. This can be explained by a simple functional description of nucleate boiling heat transfer coefficient as [40]

$$h_{nb} = S \cdot h_{pb} \quad where \quad \begin{cases} h_{pb} = f(q'') \\ S = f(G, x_e) \end{cases} \tag{12}$$

wherein the nucleate boiling heat transfer coefficient, h_{nb}, is expressed as product of the pool boiling heat transfer coefficient, h_{pb}, and 'suppression factor', S. h_{pb}, as validated from numerous pool boiling experiments, is well known interrelation that pool boiling HTC dependency on q'' is an outcome of bubble nucleation, an increased number of active nucleation sites, and intensified bubble growth rate and departure frequency. The suppression factor, S, which can be expressed as a function of mass velocity, G, and equilibrium quality, x_e, corrects the fully developed nucleate boiling prediction from h_{pb} to account for the fact that in flow boiling: (a) as the flow inertia effect increases in strength, nucleation is more strongly suppressed; and (b) as flow quality increases, convective evaporation overpowers nucleate boiling and further suppresses bubble nucleation; this is where h_{tp} shows greater sensitivity to h_{cb} rather than to h_{nb}. In conjunction, in Fig. 11, at low heat flux, regardless of the mass velocity condition, the heat transfer coefficient increased in magnitude with increasing heat flux in accordance with the pool boiling heat transfer relation. At low heat flux, due to a small vapor volume fraction, which signifies low flow quality, the suppression factor is fairly negligible and does not affect the curve trend. However, at higher heat flux where flow quality is high, the suppression factor is no longer negligible but large enough to suspend further increases of the heat transfer coefficient.

An interesting and distinct feature of cryogenic fluids is that nucleate boiling is not easily subsided but persists to preserve a high heat transfer coefficient which does not increase any further due to the dampening effect of the suppression factor until extreme heat flux very near to CHF, mainly because of cryogenic fluids' low latent heat of vaporization and surface tension. Top curves show an identical trend of curves but in a smaller magnitude of heat transfer coefficient due to the negative effect of gravitational body force causing vapor accumulation that prohibits effective heat diffusion leading to a degradation of heat transfer coefficients.

4.3.2. *Effect of phase separation parameter, $1/X_{tt}$*

It is a controversial topic whether a convective boiling regime appears in cryogenic flow boiling. Qi et al. [24] who studied liquid nitrogen flow boiling using 0.531–1.931 mm diameter microtubes, indicated that the nucleate boiling mechanism governs the low quality region while a convective boiling mechanism governs the high quality region. Shirai et al. [41] investigated liquid hydrogen and nitrogen flow boiling in 6–8 mm i.d. tubes and proposed a two-phase heat transfer coefficient developed from a pool boiling HTC correlation based on their finding that two-phase heat transfer characteristics for cryogens can be assumed to be nucleate boiling dominant without convective boiling contribution. Steiner and Schlűnder [19] experimented with liquid nitrogen flow boiling using 14-mm diameter tubes and presented a local heat transfer coefficient trend against flow quality. They found a strong dependency of heat transfer coefficient on heat flux and explained nucleate boiling to be prevalently dominant for the parameters varied in their experiments; they also noted that no pure convective boiling occurs, absent heat transfer coefficient dependence on heat flux.

Consequently, the existence of convective boiling for cryogenic flow boiling is difficult to infer or analyze only from heat transfer coefficient variations with heat flux or flow quality. In order to explicitly confirm the existence of a convective boiling mechanism in cryogenic flow boiling, a phase separation parameter, $1/X_{tt}$, can be employed, as originally proposed in the study by Chen [40]. Note that X_{tt} is the Lockhart–Martinelli parameter for turbulent liquid-turbulent vapor flows, defined as

$$X_{tt} = \left(\frac{1-x_e}{x_e}\right)^{0.9} \left(\frac{\rho_g}{\rho_f}\right)^{0.5} \left(\frac{\mu_f}{\mu_g}\right)^{0.1} \tag{13}$$

Ganesan et al. [34], who compiled a comprehensive database of heated tube flow boiling data for various cryogenic fluids and investigated two-phase heat transfer characteristics of cryogens, by employing the Chen's approach [40], established the explicit evidence for the presence of convective boiling by examining the correlation between the cryogenic two-phase heat transfer coefficient, h_{tp}, and $1/X_{tt}$. As a result of examination, they reported an intensifying relative trend between cryoenic h_{tp} and $1/X_{tt}$ for high phase separation (annular flow, $1/X_{tt} \geq 1$ [34]) than for low phase separation (bubbly flow, $1/X_{tt} < 0.1$ [34]). Moreover, based on the finding, they justified the expression of the cryogenic convective boiling HTC, h_{cb}, as a product of convective single-phase liquid HTC (associated with heat transfer across the annular liquid film in annular flow), $h_{sp,f}$, and a heat transfer 'enhancement factor', F,

$$h_{cb} = F.h_{sp,f} \tag{14}$$

where the single phase HTC is based on the Gnielinski [42] correlation,

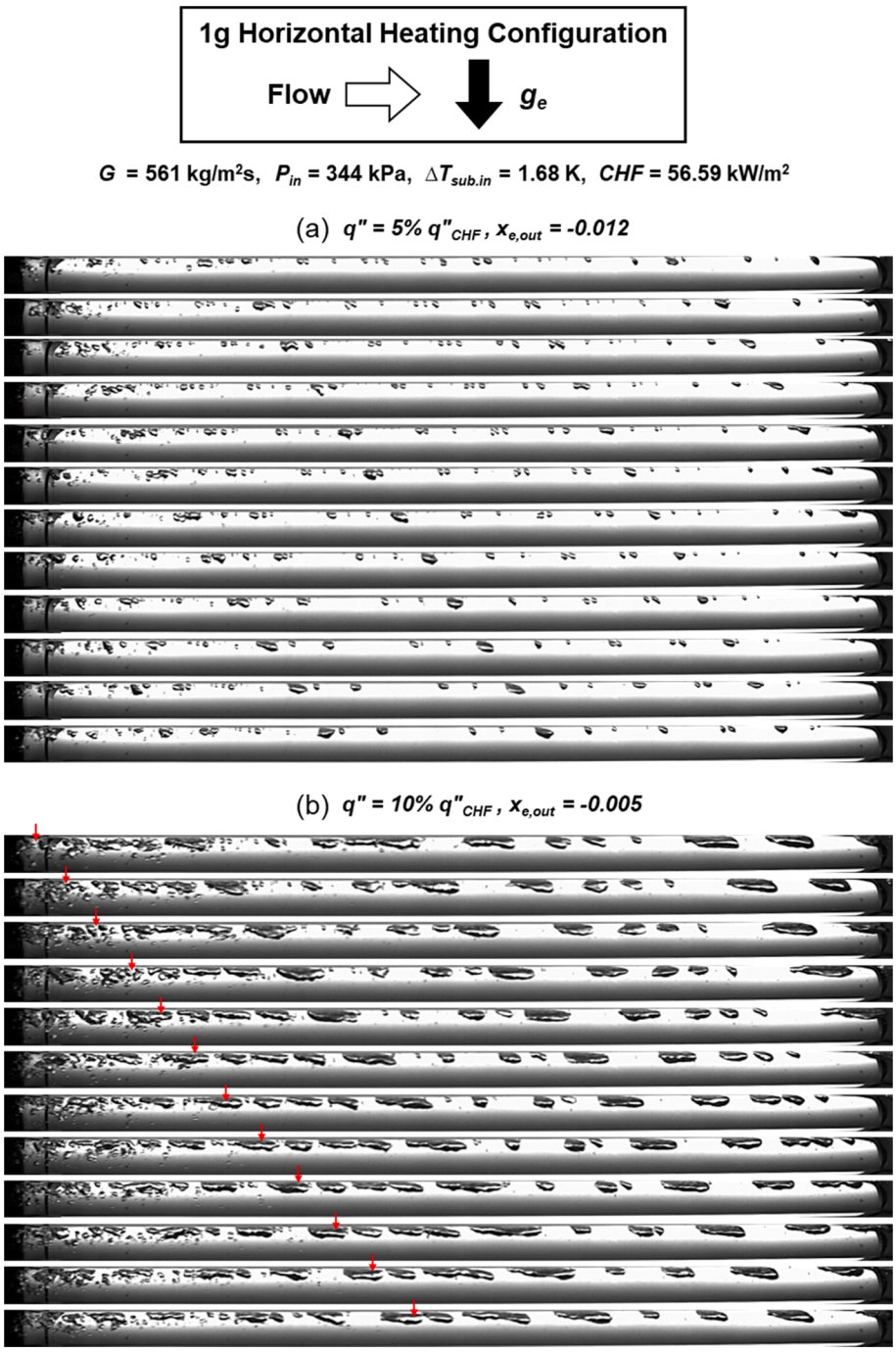

Fig. A1. Flow visualization image sequences for near-saturated inlet at mass velocities of G = 561 kg/m^{2}s at (a) 5% q''_{CHF}, (b) 10% q''_{CHF}. (Continue) Flow visualization image sequences for near-saturated inlet at mass velocities of G = 561 kg/m^{2}s at (e) 34% q''_{CHF}, (f) 60% q''_{CHF}. (Continue) Flow visualization image sequences for near-saturated inlet at mass velocities of G = 561 kg/m^{2}s at (a) 13% q''_{CHF}, (b) 19% q''_{CHF}.

$$h_{sp,f} = \frac{(4f_{sp,fo}/8)(Re_{fo,D} - 1000)Pr_f}{1 + 12.7\left(\frac{4f_{sp,fo}}{8}\right)^{0.5}(Pr_f^{2/3} - 1)}\frac{k_f}{D} \tag{15}$$

As its name suggests, the enhancement factor indicates an increasing contribution of h_{cb} to h_{tp} with increasing phase separation. It is essential to highlight that the use of the enhancement factor approach is a well-established method originally proposed by Chen [40], and Ganesan et al. [34] have provided explicit evidence and justification for applying the same method to cryogenic flow boiling.

Fig. 12(a) and 12(b) are plots of local HTC data, normalized as h_{tp}/h_{sp}, against $1/X_{tt}$ for the bottom wall and the top wall, respectively. For the bottom wall, Fig. 12(a), the data show no reliance on the phase separation parameter, $1/X_{tt}$, indicating heat transfer at the bottom of the tube is dominated by nucleate boiling rather than convective boiling. The independence of h_{tp}/h_{sp} from $1/X_{tt}$ agrees with the previously introduced flow visualizations where bubble nucleation and departure are shown to be actively taking place until high heat flux regions due to the unique thermal properties of cryogens having low surface tension and latent heat of vaporization. However, for the top wall, Fig. 12(b), as $1/X_{tt}$ increases, which implies increased phase separation, the slope of the curve begins to increase, from near zero for low values of the

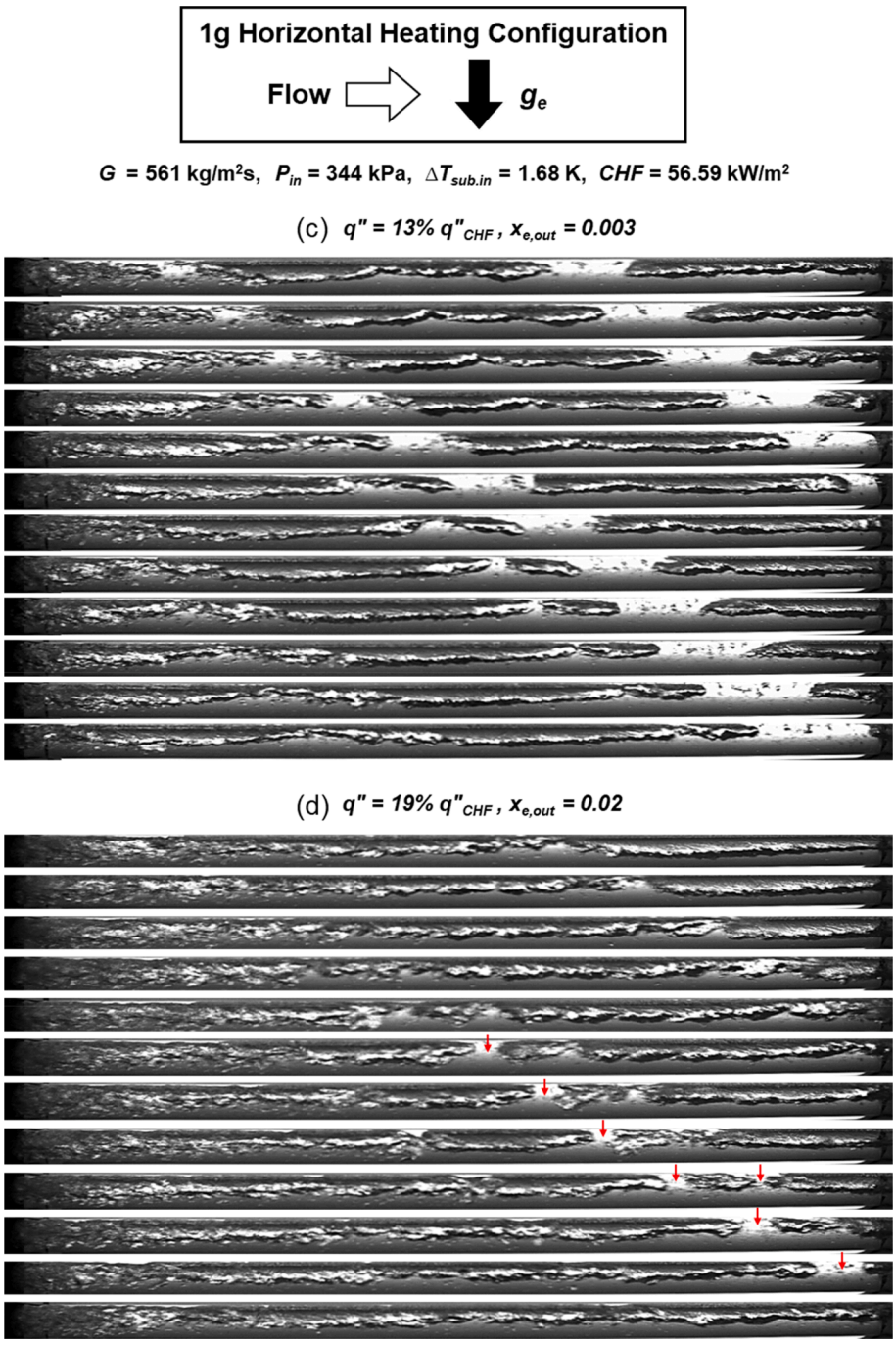

Fig. A1. (*continued*).

separation parameter ($1/X_{tt} < 0.1$) to a non-zero positive value for the intermediate range ($0.1 < 1/X_{tt} < 1$). It can be anticipated to have a continuous trend of increase of h_{tp}/h_{sp} for even higher $1/X_{tt}$ values, but due to the limited operating conditions of the present experiments, it is not possible to provide quantitative evidence in the same figure. The HTC trend in Fig. 12(b) is consistent with the earlier flow visualization results indicating formation of large vapor structures under thin liquid annulus film due to flow stratification aided by gravitational body force attenuating active bubble nucleation and departure. Therefore, by confirming the dependency of h_{tp}/h_{sp} on the separation parameter for $0.1 < 1/X_{tt} < 1$, it can be clearly stated that convective boiling coexists with nucleate boiling, contributing to heat transfer for the top wall region in 1-g_e horizontal LN_2 flow boiling.

4.3.3. *Effect of inlet pressure*

Fig. 13 shows the measured local heat transfer coefficient variation with increasing heat flux under two different inlet pressures at the axial location of $z = 505$ mm and mass velocity of $G = 845$ kg/m^{2}s. Overall, the flow boiling heat transfer coefficients are larger at higher inlet pressures than at lower inlet pressures. Also, the difference between the two pressures is not significant at lower heat fluxes but was much larger at higher heat fluxes. At higher pressures, due to a decreased surface tension, it is much easier to nucleate bubbles and easier for those nucleated bubbles to depart from the heated wall. Departed small bubbles induce turbulence and mixing effects near the heated surface, effectively assisting in heat dissipation. Therefore, the heat transfer coefficient increases at higher pressures.

In the lower heat flux range, the curves at both pressures almost

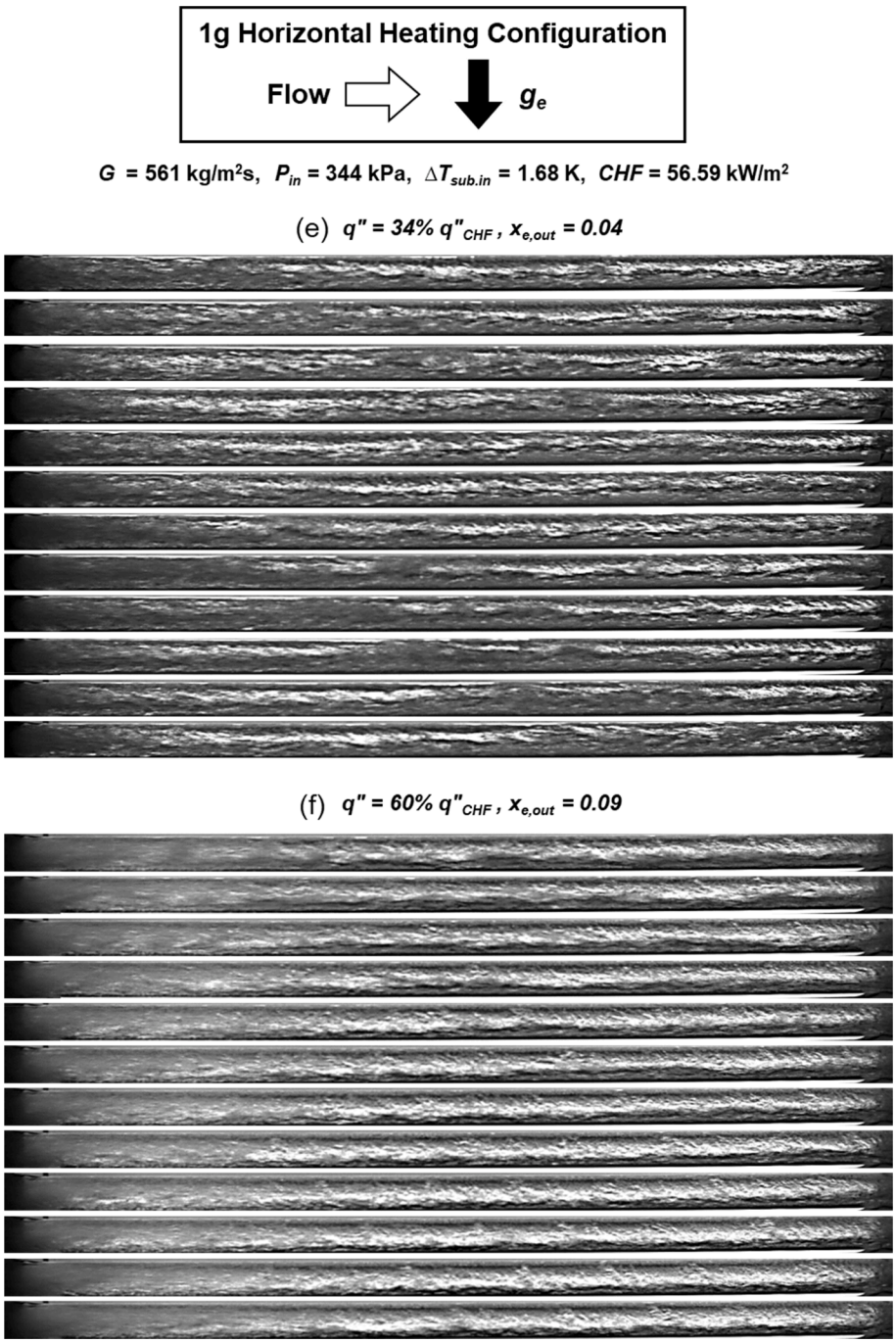

Fig. A1. (*continued*).

overlap with each other indicating appreciable contribution of single-phase liquid forced convection where pressure reliance is limited. However, as latent heat transfer becomes dominant, at heat flux higher than ~ 20 kW/m^2, the two curves begin to deviate from each other and further increases of heat flux intensify the difference. Notice, however, how the high heat flux range brings about little dependence of h_{tp} on heat flux. These pressure dependent trends are were also confirmed from Steiner and Schlűnder [19] where they found improved heat transfer with increasing pressure in the low vapor quality region but not in the high vapor quality region. Qi et al. [24] and Fang et al. [26] reported the similar trend of enhancing heat transfer coefficients with increasing pressure. Both studies explained this trend based on reduced required superheat for bubble nucleation due to the reduced surface tension as mentioned earlier. Another noteworthy observation of pressure effect on HTC found in the present study is the varying degree of pressure effect at the top and bottom surfaces. The pressure effect is larger at the bottom surface than at the top surface, as illustrated in Fig. 13. At the top surface, due to gravitational body force where vapor is accumulated and actively coalescing, the flow is already enhanced with aggressive mixing and turbulence aided by migrated bubbles from the bottom surface. Therefore, additional mixing or enhanced turbulence with increased pressure does not significantly improve heat transfer efficiency of LN_2. Notice the drop in HTC at $q''\approx$ 15 kW/m^2. The reduction is due to a lower mass velocity at that specific steady state. Despite meticulous needle valve control, rapid void fraction increase caused a slight deviation from the target mass velocity. However, for other steady states in the same case, mass velocity remains close to the target, not affecting the overall trend.

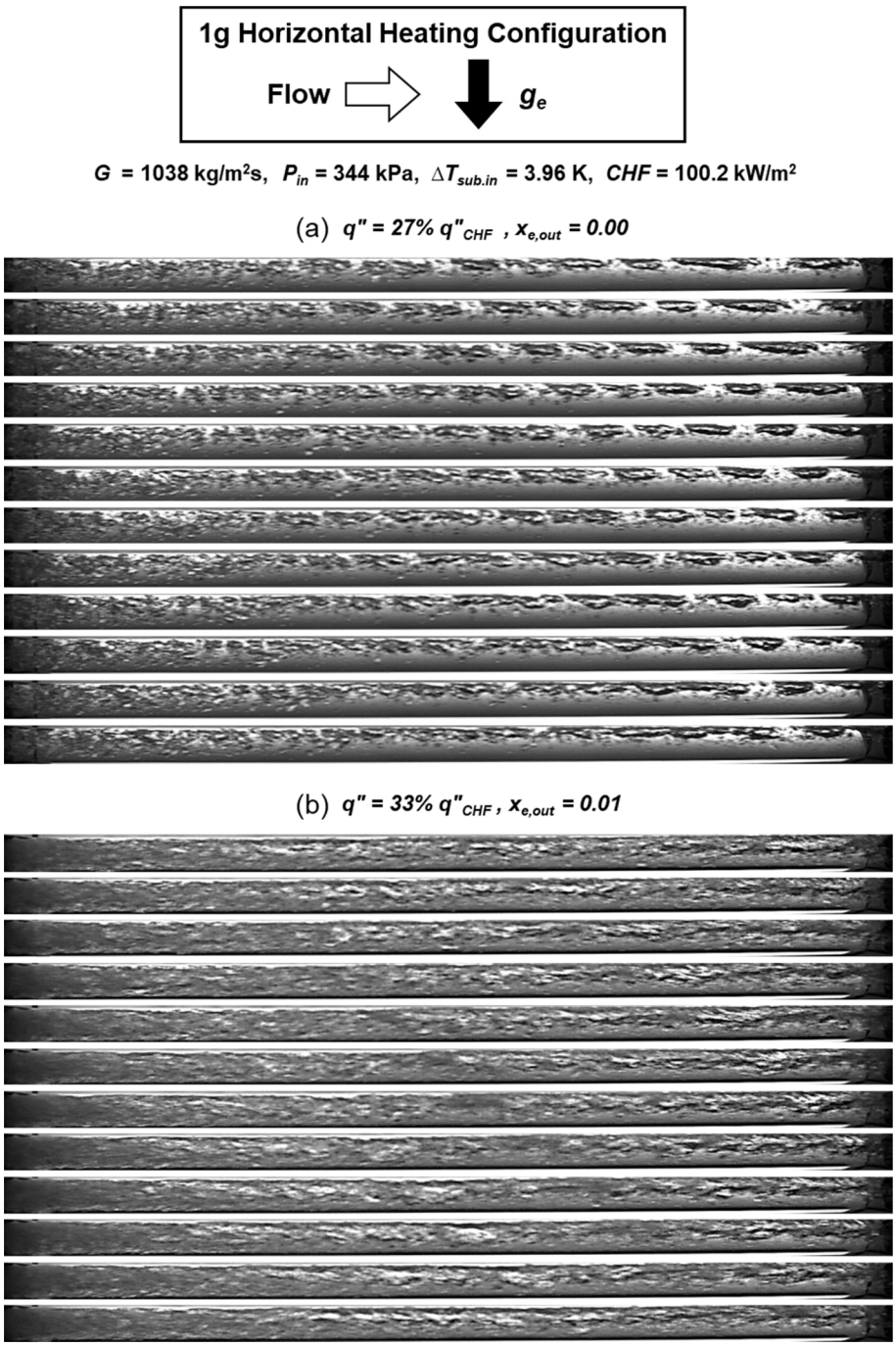

Fig. A2. Flow visualization image sequences for near-saturated inlet at mass velocities of $G = 1038$ kg/m^{2}s at (a) 27% q''_{CHF}, (b) 33% q''_{CHF}. (Continue) Flow visualization image sequences for near-saturated inlet at mass velocities of $G = 1038$ kg/m^{2}s at (c) 57% q''_{CHF}, (d) 94% q''_{CHF}.

4.4. Evaluation of seminal correlations

4.4.1. Flow boiling correlations

The performance of seminal flow boiling HTC correlations is tested and compared to the measured local heat transfer coefficients. The comparisons are conducted based on evaluating mean absolute error (MAE) which is defined for local HTC as

$$MAE = \frac{1}{N}\sum \frac{\left|h_{tp,pred} - h_{tp,meas}\right|}{h_{tp,meas}} \times 100[\%] \tag{16}$$

Eight different flow boiling correlations are evaluated against the measured data and are summarized in Table 4, segregated into different assessments for the bottom wall and top wall. Notice how these correlations can be grouped into three main categories: (i) derived specifically for pool boiling, (ii) derived from flow boiling data for different fluid types, and (ii) derived from cryogenic data alone. Note that all the presented correlations do not distinguish the top or bottom walls but provide single HTC values for each axial location. In addition, all the presented correlations do not address partial wetting of tube wall. Therefore, it is rational to have better MAE for HTC at the bottom wall than at the top wall.

In Fig. 14, parity plots are shown for the evaluated flow boiling correlations. For the bottom wall, the two best performing flow boiling

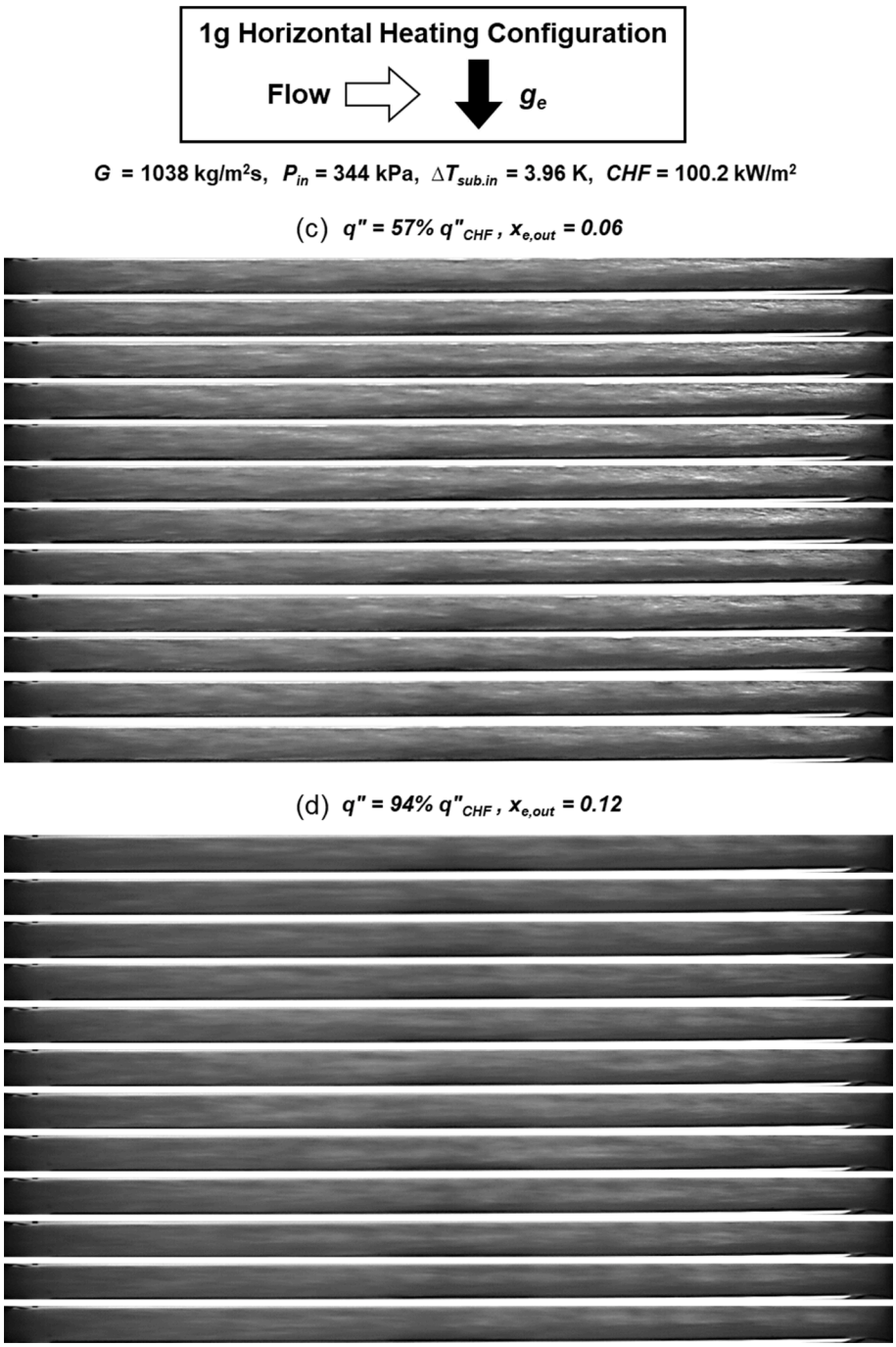

Fig. A2. (*continued*).

correlations, with MAEs of 12.21%, and 13.64%, are Steiner and Taborek [49], and Liu and Winterton [48], respectively. Despite the highest accuracy, the correlation by Steiner and Taborek [49] are deemed inferior due to its reliance on distinct empirical constants for different cryogenic fluids. Liu and Winterton's HTC correlation [48], which utilizes the functional form of Eq. (11), was developed based on nine different room temperature fluids and is designed to predict heat transfer coefficients for both vertical and horizontal orientations. The correlation from Ganesan et al. [34], which also utilizes the functional form of Eq. (11), was developed based on a consolidated flow boiling database spanning six different cryogenic fluids (including liquid nitrogen) and is designed to predict heat transfer coefficients for both vertical and horizontal orientations. For the top wall, the correlations by Liu and Winterton [48] and Ganesan et al. [34], with MAEs of 37.81% and 38.39%, respectively, provide comparatively accurate predictions for the top wall as well.

4.4.2. *Pool boiling correlations*

Performance of pool boiling HTC correlations were also tested and compared to measured local heat transfer coefficients. In Fig. 15, HTC correlations by Foster and Zuber [43] having implicit functional form, and by Cooper [44] having explicit functional form, are evaluated against the measured flow boiling data and show good to moderate MAEs for the bottom surface of 12.37% and 19.99%, respectively. However, the same correlations show relatively high MAEs for the top surface, 50.67% and 64.84%, respectively. Better predictions for the bottom surface can be explained by dominance of bubble nucleation, growth, and departure, which resemble behavior observed during pool

boiling. But, since pool boiling correlations cannot represent boiling on the underside of heated wall or development of long vapor features as top surface, the accuracy of the same correlations is compromised when compared to top surface flow boiling data from the present study.

5. CONCLUSIONS

The present study investigated flow boiling of LN_2 with a near-saturated inlet based on results obtained from Earth gravity in the horizontal orientation. Experiments were conducted using the same payload to be used in upcoming parabolic flight campaigns, with a key goal of demonstrating the robustness of the payload for parabolic flight. Acquired heat transfer results include flow boiling curves, streamwise wall temperature profiles, streamwise heat transfer coefficient profiles, and average heat transfer coefficients. Additionally, high-speed video images were acquired for various operating conditions. Unique cryogenic flow boiling trends were discussed in terms of heat flux, mass velocity, the phase separation parameter, $1/X_{tt}$, and inlet pressure. Furthermore, predictive accuracies of various seminal heat transfer coefficient correlations were assessed against the present LN_2 data. Key contributions from the study are as follows:

(1) High-speed video images, obtained in an adiabatic flow visualization tube downstream of the heat transfer test section, provided valuable insight into the dominant two-phase regimes and transitions in between. At low G, multiple flow regimes were captured: bubbly, plug, slug, stratified annular, and annular. At higher G conditions, with stronger flow inertia, the observed flow patterns were predominantly a uniform bubbly flow. As heat flux increased, the flow regime directly transitioned into annular flow, with the absence of plug or slug flow regimes.
(2) The analysis of the boiling curve revealed several key trends in cryogenic flow boiling performance: (a) a sharp increase in slope after boiling initiation, (b) a nearly vertical slope indicating dominance of nucleate boiling facilitated by continuous nucleation within the annular liquid film, (c) partial dryout of the annular liquid film leading to CHF and subsequent uncontrolled excursions in wall temperature, and (d) improved heat transfer coefficients and CHF under higher mass velocities.
(3) The initial rise in cryogenic heat transfer coefficients with increasing heat flux signifies the pronounced influence of nucleate boiling mechanism in cryogenic flow boiling.
(4) The leveling off and sustaining cryogenic heat transfer coefficient trend at high heat flux range is a direct consequence of the persisting nucleate boiling of cryogens, allowing cryogenic flow boiling to maintain a high magnitude of heat transfer coefficient until reaching CHF.
(5) The correlation observed between the phase separation parameter, $1/X_{tt}$, and the cryogenic heat transfer coefficient indicates the presence of a convective heat transfer mechanism in cryogenic flow boiling.
(6) Cryogenic heat transfer coefficients increased with increasing inlet pressure mostly because of enhanced bubble nucleation and departure aided by decreasing values of latent heat of vaporization, h_{fg}, phase density difference, $(\rho_g - \rho_f)$, and surface tension, σ, with increasing pressure.
(7) Seminal HTC correlations were evaluated for accuracy against the measured heat transfer data. The correlations by Steiner and Taborek [49], and Liu and Winterton [48] offered best predictions, with MAEs of 12.21% and 13.64%, respectively. Pool boiling correlations were also evaluated and shown to provide good to moderate predictive accuracy, given the dominance of the nucleate boiling mechanism for the operating conditions of this study.

CRediT authorship contribution statement

Sunjae Kim: Conceptualization, Data curation, Formal analysis, Investigation, Methodology, Software, Validation, Visualization, Writing – original draft, Writing – review & editing. **Nishad Damle:** Investigation, Validation, Visualization. **Issam Mudawar:** Conceptualization, Formal analysis, Funding acquisition, Investigation, Methodology, Project administration, Resources, Supervision, Visualization, Writing – original draft, Writing – review & editing. **Jason Hartwig:** Conceptualization, Funding acquisition, Investigation, Methodology, Project administration, Resources, Supervision, Writing – original draft, Writing – review & editing.

Declaration of competing interest

The authors declare that they have no known competing financial interests or personal relationships that could have appeared to influence the work reported in this paper.

Data availability

The authors are unable or have chosen not to specify which data has been used.

Acknowledgement

The authors are appreciative of the support of the National Aeronautics and Space Administration (NASA) under grant nos. 80NSSC21K0500 and 80GRC018C0055.

Appendices

a.1 Low mass velocity flow image sequence

Fig. A1(a)–(f) include high speed image sequences for a mass velocity of $G = 561$ kg/m^{2}s, $P_{in} = 344$ kPa, and $\Delta T_{sub\ in} = 1.68$ K at six different wall heat flux conditions, q" of 5%, 10%, 13%, 19%, 34%, and 60% $q"_{CHF}$. The images in each sequence are 10 ms apart. At 5% and 10% $q"_{CHF}$, discrete bubbles enter the visualization tube across the entire cross-sectional area of the tube inlet not only through the top portion of the area. The bubbles flowing through the lower half of the tube gradually ascend toward the top surface. In Fig. A1(b), indicated with red arrows, a cluster of bubbles flowing into the tube inlet are tracked with the time. With buoyancy effects, small bubbles are traveling up towards the top surface and accumulate, which can be observed from the first and second image of Fig. A1(b). However, from the second to third image of Fig. A1(b), clustered bubbles suddenly disperse and travel away from each other without being merged. According to Sharma et al. [51], small sized bubbles, when collided or densely packed due to the bubble collision dispersion force, are repelled from each other resulting in well distributed bubble concentrations across the cross-sectional area of the tube. Also, the bubble collision dispersion force was adapted into computational flow boiling simulations and was validated by the present authors [52]. From actual flow visualization in these figures, the diffusion of highly concentrated bubbles after their sudden accumulation is clearly captured. As flow proceeds, due to the overpowering of the body force and reduction of the bubble collision dispersion force effect with increasing bubble diameter, the merging of bubbles takes place and forms a vapor plug. In addition, with the absence of boiling within the visualization tube, the turbulent mixing effect is less apparent than it is in the test section where bubble nucleation and departure are active. Therefore, as bubbles proceed through the visualization section, the interface become less wavy and the variation of flow structure reduces. At 13% and 19% $q"_{CHF}$, a larger and elongated vapor structure is entering the visualization tube. In Fig. A1(d), plugs are connected due to increasing vapor generation within the test section, covering almost the

entire length of the visualization section. However, with time, due to the increased velocity difference between the phases, liquid below the vapor structure is entrained having a liquid wave span almost the entire diameter of the tube. This flow regime is consistent with slug flow. As heat flux increases up to 34%–60% $q"_{CHF}$, the flow pattern develops into annular flow having an annular liquid film around the vapor core. From Fig. A1(e) and A1(f), it is clear that waviness exists for both cases but to a lesser degree at higher heat flux due to the thinning of liquid film.

a.2 High mass velocity flow image sequence

Fig. A2(a)–(d) includes high speed image sequences for a mass velocity of $G = 1038$ kg/m^{2}s, $P_{in} = 344$ kPa, and $\Delta T_{sub\ in} = 3.96$ K at four different wall heat flux conditions, $q"$ of 27.7%, 33.1%, 57.6%, and 94.1% $q"_{CHF}$. The images in each sequence are 10 ms apart. At 27.7% $q"_{CHF}$, a great number of small and discrete bubbles are flowing into the visualization section in a well distributed fashion. Due to intensive inertia and turbulent mixing with the high mass velocity, bubbles are well scattered and are not merging until a farther axial location of the visualization section when compared to the transient flow sequence at lower mass velocities in Fig. A1(a) and A1(b). Near the outlet at the downstream of the visualization section, bubbles are coalescing to form elongated vapor structures or plugs. It is interesting that the points where those plugs appear are fixed at similar axial locations without much variation at each time. At 33.1% $q"_{CHF}$, bountiful vapor bubbles rush into the visualization tube with increased velocity forming a uniform scatter within the bulk liquid. As flow stabilizes at a further axial location, bubbles merge and project toward the top surface. This causes bulk liquid to flow downwards, compensating for the flushed vapor. Notice the violently fluctuating liquid–vapor interface having a sharp crest as shown in Fig. A2(b). The sharp edges of the wave crests shatter due to high vapor velocity entraining liquid droplets or liquid chunks within the vapor core. At higher heat flux percentages of 57.6% and 94.1% $q"_{CHF}$, due to the increased vapor generation leading to higher vapor velocities, liquid is spread outward covering the entire perimeter of the visualization tube. In the vapor core, among the fast-flowing vapor, entrained liquid strips are intermittently observed as thin linings with darker colors in the center of the tube.

References

[1] W.L. Johnson, J.R. Stephens, NASA's cryogenic fluid management technology development roadmaps, Joint Army-Navy-NASA-Air Force (JANNAF) In-Space Chemical Propulsion Technical Interchange Meeting (TIM), Huntsville, Alabama, 2018.

[2] J. Hartwig, J. Vera, Numerical modeling of the transient chilldown of a cryogenic propellant transfer line, J Thermophys Heat Transf. 30 (2016) 1–7.

[3] J. Hartwig, S. Darr, A. Asencio, Assessment of existing two phase heat transfer coefficient and critical heat flux correlations for cryogenic flow boiling in pipe quenching experiments, Int. J. Heat Mass Transf. 93 (2016) 441–463.

[4] M. Meyer, J. Hartwig, S. Sutherlin, A. Colozza, Recent concept study for cryogenic fluid management to support opposition class crewed missions to Mars, Cryogenics 129 (2023) 103622.

[5] J.C. Burke, W.R. Byrnes, A.H. Post, F.E. Ruccia, Pressurized cooldown of cryogenic transfer lines, Advances in Cryogenic Engineering 4 (1960) 378–394.

[6] J.C. Bronson, F.J. Edeskuty, J.H. Fretwell, E.F. Hammel, W.E. Keller, K.L. Meier, A. F. Schuch, W.L. Willis, Problems in cool-down of cryogenic systems, Advances in Cryogenic Engineering 7 (1962) 198–205.

[7] J.A. Brennan, E.G. Brentari, R.V. Smith, W.G. Steward, Cooldown of cryogenic transfer lines, National Bureau of Standards, NBS-9264 (1966).

[8] C. Velat, Experiments in cryogenic two phase flow Masters thesis, University of Florida, 2004.

[9] O. Kawanami, T. Nishida, I. Honda, Y. Kawashima, H. Ohta, Flow and heat transfer on cryogenic flow boiling during tube quenching under upward and downward flow, Microgravity Sci. Technol 19 (2007) 137–138.

[10] O. Kawanami, H. Azuma, H. Ohta, Effect of gravity on cryogenic boiling heat transfer during tube quenching, Int J Heat Mass Transf 50 (17–18) (2007) 3490–3497.

[11] K. Yuan, Y. Ji, J.N. Chung, W. Shyy, Cryogenic boiling and two-phase flow during pipe chilldown in earth and reduced gravity, J Low Temp Phys 150 (1–2) (2008) 101–122.

[12] H. Hu, J.N. Chung, S.H. Amber, An experimental study on flow patterns and heat transfer characteristics during cryogenic chilldown in a vertical pipe, Cryogenics 52 (2012) 268–277.

[13] S.R. Darr, H. Hu, N.G. Glikin, J.W. Hartwig, A.K. Majumdar, A.C. Leclair, J. N. Chung, An experimental study on terrestrial cryogenic transfer line chilldown I, Effect of Mass Flux, Equilibrium Quality, and Inlet Subcooling, Int J Heat Mass Transf 103 (2016) 1225–1242.

[14] S.R. Darr, H. Hu, N. Glikin, J.W. Hartwig, A.K. Majumdar, A.C. Leclair, J.N. Chung, An experimental study on terrestrial cryogenic tube chilldown II, Effect of Flow Direction with Respect to Gravity and New Correlation Set, Int J Heat Mass Transf 103 (2016) 1243–1260.

[15] S. Darr, J. Dong, N. Glikin, J. Hartwig, A. Majumdar, A. Leclair, J. Chung, The effect of reduced gravity on cryogenic nitrogen boiling and pipe chilldown, NPJ Microgravity 2 (2016) 16033.

[16] J. P. Lewis, J. H. Goodykoontz, J. F. Kline, Boiling heat transfer to liquid hydrogen and nitrogen in forced flow, NASA Technical Note, NASA-TN-D-1314, 1962.

[17] S.S. Papell, R.J. Simoneau, D.D. Brown, Buoyancy effects on critical heat flux of forced convective boiling in vertical flow, NASA Technical Report, NASA-TN-D-3672 (1966).

[18] R.J. Simoneau, F.F. Simon, A visual study of velocity and buoyancy effects on boiling nitrogen, NATA Technical Report, NASA-TN-D-3354 (1966).

[19] D. Steiner, E.U. Schlűnder, Heat transfer and pressure drop for boiling nitrogen flowing in a horizontal tube 1, Saturated Flow Boiling, Cryogenics 16 (1976) 457–464.

[20] H.M. Muller, W. Bonn, D. Steiner, Heat transfer and critical heat flux at flow boiling of nitrogen and argon within a horizontal tube, in: Advanced Course in Heat Exchangers: Theory and Practice. ICHMT Symposium, 1981, pp. 233–250.

[21] V.V. Klimenko, A.M. Sudarchikov, Investigation of forced flow boiling of nitrogen in a long vertical tube, Cryogenics 23 (1983) 379–385.

[22] V.V. Klimenko, M.V. Fyodorov, Y.A. Fomichyov, Channel orientation and geometry influence on heat transfer with two-phase forced flow of nitrogen, Cryogenics 29 (1989) 31–36.

[23] S.L. Qi, P. Zhang, R.Z. Wang, L.X. Xu, Flow boiling of liquid nitrogen in micro-tubes: Part I - The onset of nucleate boiling, two-phase flow instability and two-phase flow pressure drop, Int J Heat Mass Transf 50 (25–26) (2007) 4999–5016.

[24] S.L. Qi, P. Zhang, R.Z. Wang, L.X. Xu, Flow boiling of liquid nitrogen in micro-tubes: Part II - Heat transfer characteristics and critical heat flux, Int J Heat Mass Transf 50 (25–26) (2007) 5017–5030.

[25] X. Fu, S.L. Qi, P. Zhang, R.Z. Wang, Visualization of flow boiling of liquid nitrogen in a vertical mini-tube, Int J Multiphase Flow 34 (2008) 333–351.

[26] X. Fang, A.M. Sudarchikov, Y. Chen, A. Dong, R. Wang, Experimental investigation of saturated flow boiling heat transfer of nitrogen in a macro-tube, Int J Heat Mass Transf 99 (2016) 681–690.

[27] M.T. Lebon, C.F. Hammer, J. Kim, Gravity effects on subcooled flow boiling heat transfer, Int J Heat Mass Transf 128 (2019) 700–714.

[28] I. Mudawar, Flow Boiling and Flow Condensation in Reduced Gravity, Advances in Heat Transfer 49 (2017) 225–306.

[29] G.P. Celata, Flow boiling heat transfer in microgravity: Recent results, Microgravity Sci. Technol 19 (2007) 13–17.

[30] A. Salim, C. Colin, M. Dreyer, Experimental investigation of a bubbly two-phase flow in an open capillary channel under microgravity conditions, Microgravity Sci. Technol. 22 (2010) 87–96.

[31] C. Colin, J. Fabre, A. Kamp, Turbulent bubbly flow in pipe under gravity and microgravity conditions, J Fluid Mechanics 711 (2012) 469–515.

[32] H. Ohta, Heat transfer mechanisms in microgravity flow boiling, Annals of the New York Academy of Sciences 974 (2002) 463–480.

[33] Y. Zhang, B. Liu, J. Zhao, et al., Experimental study of subcooled flow boiling heat transfer on a smooth surface in short-term microgravity, Microgravity Sci. Technol. 30 (2018) 793–805.

[34] V. Ganesan, R. Patel, J. Hartwig, I. Mudawar, Review of databases and correlations for saturated flow boiling heat transfer coefficient for cryogens in uniformly heated tubes, and development of new consolidated database and universal correlations, Int J Heat Mass Transf. 179 (2021) 121656.

[35] H. Zhang, I. Mudawar, M.M. Hasan, Flow boiling CHF in microgravity, Int J Heat Mass Transf 48 (2005) 3107–3118.

[36] E.W. Lemmon, M.L. Huber, M.O. McLinden, NIST Standard Reference Database 23: Reference Fluid Thermodynamic and Transport Properties-REFPROP, Version 10.0, Gaithersburg, 2018.

[37] N.T. van Dresar, J.D. Siegwarth, Near-horizontal, two-phase flow patterns of nitrogen and hydrogen at low mass and heat flux, NASA-TP-2001-210380-CD, 2001. NASA Technical Report,.

[38] V. Ganesan, R. Patel, J. Hartwig, I. Mudawar, Universal critical heat flux (CHF) correlations for cryogenic flow boiling in uniformly heated tubes, Int J Heat Mass Transf 166 (2021) 120678.

[39] S. Baek, I. Park, Y. Jung, S. Jeong, Cool-down characteristics of liquid nitrogen transfer line, Proc. 8th KSME-JSME Therm. Fluids Eng. Conf., Incheon, South Kora, 2012.

[40] J.C. Chen, Correlation for boiling heat transfer to saturated fluids in convective flow, Industrial & Engineering Chemistry Process Design and Development 5 (3) (1966) 322–329.

[41] Y. Shirai, M. Shiotsu, T. Matsumoto, H. Kobayashi, Y. Naruo, S. Nonaka, Y. Inatani, Heat transfer characteristics of liquid hydrogen flowing inside of a vertical heated pipe under quasi-stationary heat input, Cryogenics 113 (2021) 103230.

[42] V. Gnielinski, Force convection in ducts, Hemisphere Handbook of Heat Exchanger Design, Hemisphere, New York, 1990.

[43] H.K. Forster, N. Zuber, Dynamics of vapor bubbles and boiling heat transfer, AIChE Journal 1 (4) (1955) 531–535.
[44] M.G. Cooper, Saturation nucleate pool boiling - a simple correlation, First U.K. National Conference on Heat Transfer, Elsevier, (1984) 785–793.
[45] M.M. Shah, Prediction of heat transfer during boiling of cryogenic fluids flowing in tubes, Cryogenics 24 (1984) 231–236.
[46] K.E. Gungor, R.H.S. Winterton, A general correlation for flow boiling in tubes and annuli, Int J Heat Mass Transf 29 (1986) 351–358.
[47] V.V. Klimenko, A generalized correlation for two-phase forced flow heat transfer—second assessment, Int J Heat Mass Transf 33 (10) (1990) 2073–2088.
[48] Z. Liu, R.H.S. Winterton, A general correlation for saturated and subcooled flow boiling in tubes and annuli, based on a nucleate pool boiling equation, Int J Heat Mass Transf 34 (11) (1991) 2759–2766.
[49] D. Steiner, J. Taborek, Flow boiling heat transfer in vertical tubes correlated by an asymptotic model, Heat Transfer Engineering 13 (2) (1992) 43–69.
[50] S.M. Kim, I. Mudawar, Universal approach to predicting saturated flow boiling heat transfer in mini/micro-channels – Part II, Two-Phase Heat Transfer Coefficient, Int J Heat Mass Transf 64 (2013) 1239–1256.
[51] S.L. Sharma, T. Hibiki, M. Ishii, C.S. Brooks, J.P. Schlegel, Y. Liu, J.R. Buchanan, Turbulence-induced bubble collision force modeling and validation in adiabatic two-phase flow using CFD, Nucl Eng and Design 312 (2017) 399–409.
[52] S. Kim, J. Lee, J. Hartwig, I. Mudawar, Computational investigation of vertical upflow boiling of liquid nitrogen and effects of bubble collision dispersion force, Int J Heat Mass Transf 203 (2023) 123780.